Journal of Solid State Chemistry **150,** 43–61 (2000)
doi:10.1006/jssc.1999.8547, available online at http://www.idealibrary.com on IDEAL®

Octahedral Tilting and Cation Ordering in Perovskite-Like $Ca_4Nb_2O_9 = 3 \cdot Ca(Ca_{1/3}Nb_{2/3})O_3$ Polymorphs

I. Levin, L. A. Bendersky, J. P. Cline, R. S. Roth, and T. A. Vanderah

Materials Science and Engineering Laboratory, National Institute of Standards and Technology, Gaithersburg, Maryland 20899
E-mail: igor.levin@nist.gov

Received June 23, 1999; in revised form October 5, 1999; accepted October 22, 1999

Four $Ca_4Nb_2O_9$ polymorphs with perovskite-related $A(B'_{1/3}B'_{2/3})O_3$ structures and different arrangements of *B*-site cations were identified and characterized by X-ray powder diffraction and transmission electron microscopy. The *B*-cation ordering in three of these phases is combined with $b^-b^-c^+$ octahedral tilting. Two high-temperature forms of $Ca_4Nb_2O_9$ are separated by a displacive phase transition which involves octahedral tilting and occurs between 1500 and 1600°C. Above this transition, the structure is either disordered or exhibits chemical 1 : 1 ordering (ordering vector $1/2[1\,1\,1]^*_c$) of Ca and Nb cations on the *B*-sites; the correct structural model has yet to be determined. Below the transition, the structure exhibits 1 : 1 ordering combined with octahedral tilting. Upon cooling, the 1 : 1 ordered structure transforms to a metastable *P*1 triclinic structure with lattice parameters $\sqrt{6}a_c \times \sqrt{2}a_c \times 2\sqrt{2}a_c$, $\alpha \approx \delta \approx 90°$, $\beta \approx 125°$ (a_c refers to cubic perovskite) and ordering vector $1/4[1\,1\,1]^*_c$. This transformation occurs by reordering of cations on (1 1 1) planes. The metastable *P*1 structure transforms upon annealing to a stable 2 : 1 ordered $P2_1/c$ structure with lattice parameters $\sqrt{6}a_c \times \sqrt{2}a_c \times 3\sqrt{2}a_c$, $\beta = 125°$ (ordering vector $1/3[1\,1\,1]^*_c$). This first-order transition occurs by precipitation and growth of the 2 : 1 ordered phase, which is stable below 1400°C. © 2000 Academic Press

Key Words: **perovskite; octahedral tilting; cation ordering; 1 : 1 ordering; 2 : 1 ordering; TEM; microstructure; $Ca_4Nb_2O_9$; phase transitions.**

INTRODUCTION

Complex titania/niobia-based oxides are of potential interest as dielectric ceramics for use in wireless communications. These ceramic materials must exhibit a combination of a high relative permitivity (ε), a low dielectric loss (tan δ), and a near-zero temperature coefficient of the resonant frequency, τ_f. The $CaTiO_3$–$Ca_4Nb_2O_9$ system is of interest because the opposite signs of τ_f for $CaTiO_3$ ($\varepsilon \approx 105$, $\tau_f = +800$ ppm/°C) and $Ca_4Nb_2O_9$ ($\varepsilon \approx 29$, $\tau_f = -22$ ppm/°C) (1) suggest the possibility of tuning τ_f to zero. The crystal structure of $CaTiO_3$ (distorted perovskite) has been studied extensively, and its room-temperature form was described by the *Pnma* (no. 62) space group with lattice parameters $a \approx a_c\sqrt{2}$, $b \approx 2a_c$, and $c \approx a_c\sqrt{2}$ (subscript "c" refers to cubic perovskite); the distortion from the ideal cubic $Pm\bar{3}m$ symmetry has been attributed to octahedral tilting (2–4). In contrast, only limited information on the structure of $Ca_4Nb_2O_9$ exists in the literature. Hervieu *et al.* (5) reported the existence of a high-temperature ($T > 1400$°C) orthorhombic ($a = 11.53$ Å, $b = 16$ Å, and $c = 11.12$ Å) form and a low-temperature ($T < 1400$°C) monoclinic ($a = 9.8$ Å, $b = 5.53$ Å, $c = 17.28$ Å, and $\beta = 125.3°$) form of $Ca_4Nb_2O_9$. They proposed that both $Ca_4Nb_2O_9$ polymorphs are derivatives of the cubic perovskite structure with one fourth of the Ca ions occupying *B* sites, i.e., $Ca(Ca_{1/3}Nb_{2/3})O_3$. For the high-temperature phase, both X-ray powder (XRPD) and selected area electron diffraction (SAED) patterns revealed superlattice reflections at $\mathbf{k} = 1/4[1\,1\,1]^*_c$ (asterisk indicates reciprocal space); however, no detailed structural analysis was conducted. The low-temperature monoclinic phase, with lattice parameters related to those of cubic perovskite by $a_m \approx a_c\sqrt{6}$, $b_m \approx a_c\sqrt{2}$, and $c_m \approx 3a_c\sqrt{2}$, displayed superlattice reflections at $\mathbf{k} = 1/6[1\,1\,1]^*_c$; the symmetry of this structure has been described by the $P2_1/c$ space group. Hervieu *et al.* (5) proposed a structure with 2 : 1 ordering of Ca/Nb cations on the octahedral *B* sites with an ordering vector $\mathbf{k} = 1/3[1\,1\,1]^*_c$. Although, the dielectric properties of $Ca_4Nb_2O_9$ are reported in Ref. (1), the structural nature of the measured specimen was not described.

The present contribution describes the results of a detailed microstructural and crystallographic study of $Ca_4Nb_2O_9$. X-ray powder diffraction and transmission electron microscopy were used to elucidate the crystal structures of the $Ca_4Nb_2O_9$ polymorphs and the phase transitions between them.

EXPERIMENTAL METHODS

The $Ca_4Nb_2O_9$ specimens were synthesized by solid-state reaction in air of $CaCO_3$ and optical-grade Nb_2O_5. Before

0022-4596/00 $35.00
Copyright © 2000 by Academic Press
All rights of reproduction in any form reserved.

TABLE 1
Schedule of Heat-Treatments

Specimen	Heat-treatment	Observed ordering
A	1600°C (18) → QW	$1/4[111]_c^*$, diffuse
B	1600°C (10) $\overset{FC}{\rightarrow}$ 1425°C → QW	$1/4[111]_c^*$, diffuse
C	A + 1000°C (10 min)	$1/4[111]_c^*$, developed
D	1400°C (15) → QW	$1/6[111]_c^*$, developed
E	1600°C (18) $\overset{FC}{\rightarrow}$ 1400°C $\overset{9\ min}{\rightarrow}$ 1200°C-QA	$1/4[111]_c^*$, developed + $1/6[111]_c^*$, precipitates
F	E + 1300°C (1) → FC	$1/4[111]_c^*$, developed
G	E + 1300°C (3) + 1450°C (10) → QA	$1/4[111]_c^*$, diffuse
H	A + 1000°C (66) → FC	$1/6[111]_c^*$, developed

Note. "QW" and "QA" refer to water and air quench, correspondingly. "FC" refers to furnace cooling with a rate of about 300°C/min. The numbers in brackets refer to a dwell time at the corresponding temperature. The observed ordering refers to superlattice reflections as observed in either electron or X-ray diffraction patterns.

each heating, mixtures were ground 15–20 min using an agate mortar and pestle; the initial grinding was carried out as an ethanol slurry. Mixtures were pressed into pellets and placed on beds of sacrificial powder of the same composition on Pt foil supported in alumina combustion boats. After an initial overnight calcine at 1000°C, reactions were completed by multiple heatings at 1375–1425°C. The details of the final heat-treatments for different specimens are summarized in Table 1.

Samples were characterized by XRPD using an automated diffractometer equipped with incident Soller slits, theta compensating slits, a 0.2 mm receiving slit, a graphite monochromator, and a scintillation detector. Data were collected at ambient temperatures using Cu$K\alpha$ radiation with a 0.02° 2θ step size and a 2-s count time. XRD data for Rietveld analysis were collected on a Siemens D500[1] diffractometer equipped with a focusing Ge incident beam monochromator, a sample spinner, and a scanning position-sensitive detector (PSD). Copper $K\alpha_1$ radiation was used. The scan range was from 15° to 155° 2θ. The data collection time was 4 h; however, the PSD offers a counting rate roughly an order of magnitude greater than conventional detectors. GSAS (6) was used for a Rietveld structural refinement as outlined by Cline (7).

The specimens for transmission electron microscopy were prepared from pellets by conventional polishing, dimpling, and ion thinning. The specimens were examined using a Phillips 430 TEM microscope operated at 200 kV. Structural imaging was performed with a JEOL 3010-UHR microscope operated at 300 kV.

[1]The use of brand or trade names does not imply endorsement of the product by NIST.

RESULTS

The present experimental results indicate the existence of four distinct $Ca_4Nb_2O_9$ perovskite-like polymorphs which feature three different arrangements of Ca/Nb cations on the *B*-sites. Two polymorphs, further referred to as the high-temperature phases, HTP_1 and HTP_2, are related by a displacive phase transition which occurs between 1500 and 1600°C. This transition involves octahedral tilting similar to that of $CaTiO_3$. X-ray powder diffraction analysis of the quenched specimens suggested that the HTP_1 and HTP_2 forms exhibit cubic and monoclinic ($\sqrt{2}a_c \times \sqrt{2}a_c \times 2a_c$, $\beta \approx 90°$) structures, respectively. Two other $Ca_4Nb_2O_9$ structures evolve from the HTP_2 at $T < 1400$°C, $LT_{1/6}$ with lattice parameters $\sqrt{6}a_c \times \sqrt{2}a_c \times 3\sqrt{2}a_c$, $\beta = 125°$; and $LT_{1/4}$ with lattice parameters $\sqrt{6}a_c \times \sqrt{2}a_c \times 2\sqrt{2}a_c$, $\alpha \approx \beta \approx 90°$, $\beta = 125°$. The $LT_{1/6}$ and the $LT_{1/4}$ structures feature superlattice reflections at $1/6[1\,1\,1]_c^*$ and $1/4[1\,1\,1]_c^*$, respectively. The $LT_{1/4}$ phase develops on cooling from $T > 1400$°C, but apparently it is metastable and transforms to the stable $LT_{1/6}$ structure after subsequent annealing at $T \leq 1400$°C. The experimental results on all four polymorphs and phase transitions between them are detailed below.

High-Temperature Phases of $Ca_4Nb_2O_9$ ($T > 1400$°C)

The XRPD patterns of specimens quenched from $T > 1400$°C (specimens A, B, and G) could be indexed using an orthorhombic unit cell with approximate lattice parameters $\sqrt{2}a_c \times \sqrt{2}a_c \times 2a_c$ (Fig. 1), similar to that of the room-temperature form of $CaTiO_3$ (*Pbnm*, no. 62, nonstandard **cab** setting (8)). Reflection conditions in the XRPD pattern are $(h\,0\,l) \rightarrow h + l = 2n$, $(h\,0\,0) \rightarrow h = 2n$, $(0\,k\,0)k = 2n$; $(0\,0\,l) \rightarrow l = 2n$. These conditions are consistent with a monoclinic $P1(2_1/n)1$ (no. 14, setting 2) structure with lattice parameters $\sqrt{2}a_c \times \sqrt{2}a_c \times 2a_c$, $\beta \approx 90°$. The nonstandard setting of axes for this structure is used to emphasize its relation to the *Pbnm* structure of $CaTiO_3$. If the absence of $(0k0)$, $k = 2n + 1$ reflections is not due to symmetry, the $Pmn2_1$ and *Pmnm* orthorhombic space groups should be also considered. Note that the *Pbnm* space group of $CaTiO_3$ would require additional reflection condition $(0\,k\,l) \rightarrow k = 2n$. Electron diffraction patterns from the quenched specimens show the presence of diffuse $1/4[1\,1\,1]_c^*$ reflections, not detected by XRPD (Fig. 2). These reflections are associated with the $LT_{1/4}$ phase which evolves from the HTP_2 on cooling and will be discussed later. If these diffuse $1/4[1\,1\,1]_c^*$ reflections are ignored, the reciprocal lattice as reconstructed from electron SAD patterns is fully consistent

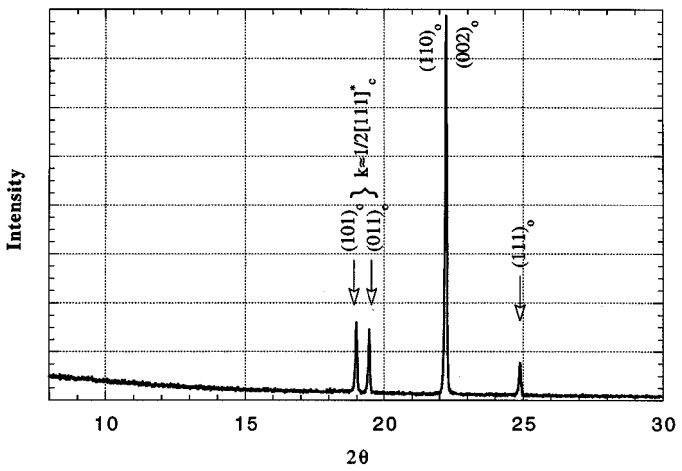

FIG. 1. Low-angle portion of the XRPD pattern from specimen A. The reflections are indexed according to an orthorhombic $\sqrt{2}a_c \times \sqrt{2}a_c \times 2a_c$ unit cell, where a_c refers to cubic perovskite.

with the symmetries derived from the XRPD. The effect of dynamical double diffraction was eliminated by careful tilting of a specimen to demonstrate the extinctions.

The microstructures of the specimens water quenched from $T > 1400°C$ (specimens A and B) consist of domains representing different crystallographic variants (with respect to a cubic lattice) of the same phase (Fig. 3). These domains can be classified in two types as follows. The type I domains (largest in size) can be considered as representing three rotational variants with different orientations of the $\mathbf{c}_o$ axis ($\mathbf{c}_o$ refers to the orthorhombic $\sqrt{2}a_c \times \sqrt{2}a_c \times 2a_c$ unit cell). In the specimens quenched from $T > 1500°C$ (specimen A), these domains (**1** and **2** in Fig. 4) are often separated by zig-zag-like interfaces with $\{110\}_c$ facets. The type I domains are subdivided into a set of alternating domains of type II ($\mathbf{1}_1$, $\mathbf{1}_2$, $\mathbf{2}_1$, $\mathbf{2}_2$) (Fig. 4). The type II domains have a common $\mathbf{c}_o$ axis but differ in the orientation of the $\mathbf{a}_o$ and $\mathbf{b}_o$ axes ($\mathbf{a}_{o1} \| \mathbf{b}_{o2}$, $\mathbf{b}_{o1} \| \mathbf{a}_{o2}$). The type II domains are separated by an interface approximately parallel to $\{001\}_c$ planes and containing the $\mathbf{c}_o$-axis. The twin character of these domains is apparent from the splitting of reflections in the corresponding SAD patterns. Similar type I and type II rotational domains have been reported for $CaTiO_3$, and their spatial hierarchy was attributed to the sequential symmetry reductions cubic → tetragonal → orthorhombic, each resulting from a different octahedral tilting (3). Alternating $\mathbf{1}_1$ and $\mathbf{1}_2$ domains are separated from the $\mathbf{2}_1$ domain by interfaces along the $(110)_c$ and $(1\bar{1}0)_c$ planes, respectively, thus producing a zig-zag appearance of the interface between domains **1** and **2**. In the quenched specimens, triangular domains bounded by interfaces parallel to $(1\bar{1}0)_c$, $(110)_c$, and $(001)_c$ planes, separating domain $\mathbf{1}_2$ from domains $\mathbf{2}_1$, $\mathbf{2}_2$, and $\mathbf{1}_1$,

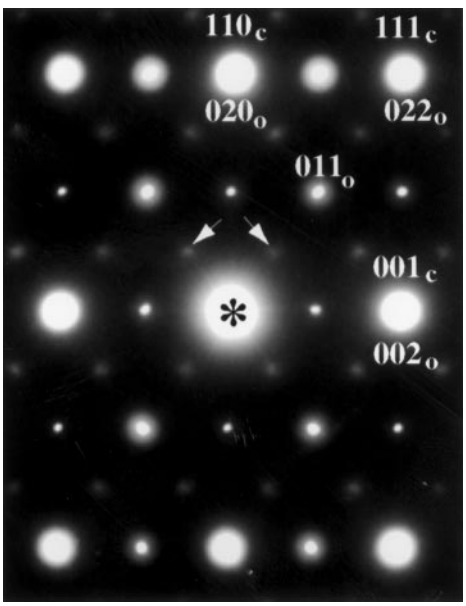

FIG. 2. SAD pattern from a single grain in specimen A in a zone axis orientation parallel to $\langle 1\,1\,0 \rangle_c$. The strong reflections are indexed according to the orthorhombic $\sqrt{2}a_c \times \sqrt{2}a_c \times 2a_c$ unit cell. Additional weak diffuse reflections at $\mathbf{k} = 1/4[1\,1\,1]_c^*$ are observed and indicated by arrows. These weak reflections are from a low-temperature polymorph, which occurs in the high-temperature form even after the fastest quenching.

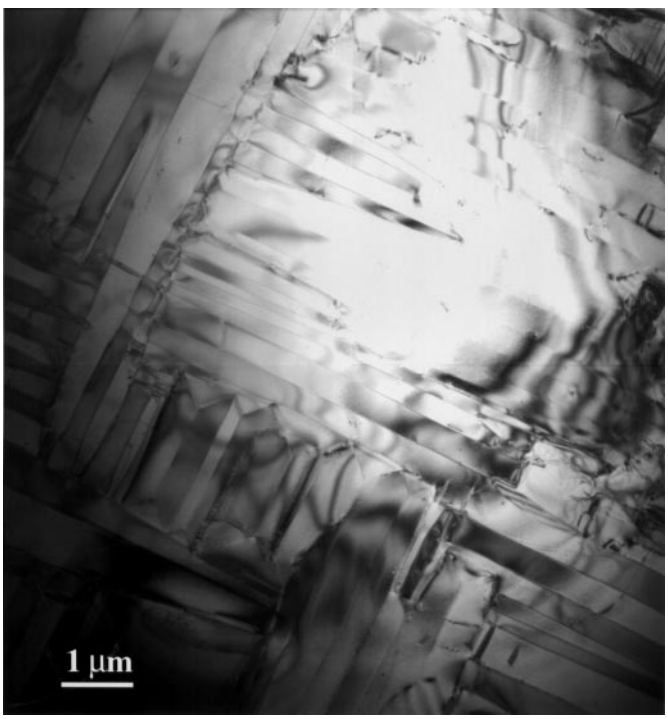

FIG. 3. Bright-field image of rotational domains in the specimen water quenched from 1600°C (specimen A).

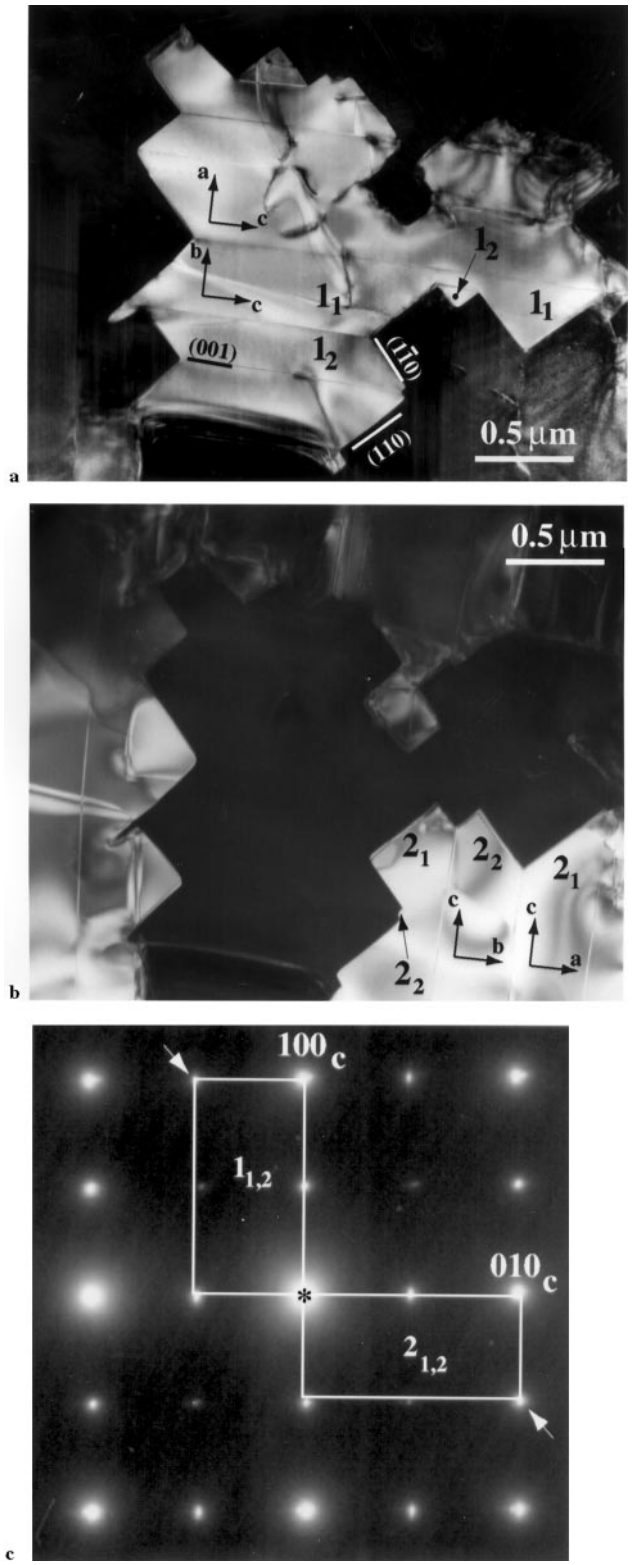

FIG. 4. (a, b) Dark field images of the type I and type II rotational domains in the specimen water quenched from 1600°C (specimen A) and (c) the corresponding SAD pattern. The dark field images in (a) and (b) were recorded close to two-beam conditions with reflections indicated by the arrows in (c).

correspondingly, were typically observed (Fig. 3). In all cases, the interdomain boundaries tend to form triple junctions. Slower cooling (specimens B, E) results in a coarsening of primary domains and loss of $\{1\,1\,0\}_c$-type faceting.

The high-temperature forms of $Ca_4Nb_2O_9$ were not completely quenchable (Fig. 2); therefore, rigorous structure determination requires diffraction data obtained at $T > 1400$°C. In the absence of such data, the structural models were determined from characterization of quenched specimens and certain assumptions, as follows.

The presence of twin-related orthorhombic domains in specimens quenched from $T > 1500$°C indicates the occurrence of a phase transition on cooling. Both the kinetics of domain formation and the domain morphology suggest a displacive-type phase transition. By analogy with known perovskite-like ABO_3 structures, which have tolerance factors[2] $t < 1$, we attributed the displacive transitions in $Ca_4Nb_2O_9$ ($t = 0.85$ assuming random occupation of the B site by Ca/Nb) to the octahedral tilting.

A classification scheme for ABO_3 structures which related all the possible (23) tilt systems to the resulting space groups was proposed by Glaezer (10) and Alexandrov (11), but neither of these space groups is compatible with *all* extinctions as observed by XRPD. In fact, there are only five tilt systems which result in a $\sqrt{2}a_c \times \sqrt{2}a_c \times 2a_c$ orthorhombic or pseudo-orthorhombic lattice, $a^-b^-c^+$ (space group $P112_1/m$), $b^-b^-c^+$ (*Pbnm*), $b^-b^-a^-$ (*I*2/*c*), $a^0b^-b^-$ (*Imcm*), and $a^0b^-c^-$ (*I*2/*m*) (10–12). Based on the extinction criteria, only *Imma*, *Pbnm*, *I*2/*a*, and *I*2/*m* have the *n*-glide symmetry planes needed to account for some reflection conditions. According to a recent compilation by Woodward (14), no structures with $a^-b^-b^-$ octahedral tilt have been reported, while very few structures exhibit $a^0b^-b^-$ and $a^0b^-c^-$ tilts (13). In contrast, the $b^-b^-c^+$ (*Pbnm*) tilt system was observed for numerous perovskite-based structures with $t < 0.975$ (e.g., $CaTiO_3$) (13). Based on the above considerations, we selected the $b^-b^-c^+$ tilt system as the most probable octahedral tilting in a high-temperature form of $Ca_4Nb_2O_9$.

From the three space groups ($P1(2_1/n)1$, $Pmn2_1$, and *Pmnm*) which fit the reflection conditions, only the $Pmn2_1$ and the $P1(2_1/n)1$ are consistent with the $b^-b^-c^+$ tilt, suggested by the above considerations. The structure with $Pmn2_1$ symmetry can be derived from the ABO_3 structure with an $b^-b^-c^+$ tilt system (*Pbnm*) *only* by introducing additional displacements of A cations, incompatible with the symmetry of octahedral tilted framework. In contrast, a $P1(2_1/n)1$ structure can be derived from the *Pbnm* structure with $b^-b^-c^+$ tilt by applying 1:1 (NaCl-type) type

[2]The tolerance factor for a perovskite ABO_3 structure is defined as $t = (R_A + R_O)/\sqrt{2}(R_B + R_O)$, where R_A, R_B, and R_O are radii of A, B, and O ions, respectively (9).

ordering of B cations, ordering vector $\mathbf{k} = 1/2\langle 1\,1\,1\rangle_c^*$. This type of ordering has been observed in $A(B'_{1/3}B''_{2/3})X_3$ compounds and results in a partially ordered structure with alternating $\{111\}_c$ planes occupied exclusively by B'' cations and a random mixture of B' and the remaining B'' cations (14). In the absence of octahedral tilting, 1:1 ordering creates a superstructure with $Fm\bar{3}m$ symmetry, lattice parameter $a = 2a_c$, and superlattice reflections at $\mathbf{k} = 1/2[111]_c^*$. This arrangement is also observed for the high-temperature form of $Sr_4Nb_2O_9$ (15). A combination of both 1:1 ordering and $b^-b^-c^+$ tilt is incompatible with an orthorhombic lattice and results in a monoclinic (pseudo-orthorhombic) $P1(2_1/n)1$ structure with lattice parameters $2a_c \times \sqrt{2}a_c \times \sqrt{2}a_c$, $\beta \neq 90^\circ$ (Fig. 5). Similar structures were reported for elpasolite-type compounds (16, 17). Figure 5 illustrates the change in equivalency of B-sites in going from the disordered Pbnm structure to a 1:1 ordered arrangement. This change eliminates both the b-glide and the mirror symmetry planes, thus reducing the symmetry from $Pbnm$ to $P1(2_1/n)1$. Formally, the $P1(2_1/n)1$ space group can be derived by a continuous reduction in symmetry from $Pm\bar{3}m$ through the 1:1 ordered $Fm\bar{3}m$ by imposing symmetry changes due to a $b^-b^-c^+$ tilt system.

We refined both $P2_1/n$ (1:1 ordered) and $Pmn2_1$ (disordered) structural models using X-ray powder data from a specimen that had been quenched in water from 1600°C. The initial atomic positions for both models were those reported for orthorhombic $CaTiO_3$ (2). The 1:1 ordering of Ca and Nb cations was imposed for the $P2_1/n$ model. The scale factor, zero correction, lattice parameters, peak profile parameters, and free parameters of atomic positions were refined. The structural changes responsible for the diffuse $1/4[111]_c^*$ reflections from a lower temperature polymorph (detected by electron diffraction and not visible in XRPD patterns) were omitted, and therefore no refinement of temperature factors was attempted. The results of the refinement clearly indicated that the $P2_1/n$ model ($R_{wp} = 11.1\%$) with 1:1 ordering of the B-cations is far superior to the disordered $Pmn2_1$ ($R_{wp} = 21\%$) model. Both experimental and calculated X-ray patterns for the $P2_1/n$ model are given in Fig. 6, while the refined atomic positions are given in Table 2. The maximal to minimal B–O bond length ratios were 1.011 and 1.017 for the $B'O_6$ ($B' = Nb$) and $B''O_6$ ($B'' = Ca/Nb$) octahedra, respectively, indicating nearly regular octahedra. The average B'-O and B''–O distances were 2.02 and 2.16 Å, respectively, consistent with the larger average radius of B'' sites occupied by a disordered mixture of Ca and Nb cations. The tilting angles for c^+ and b^-b^- tilts in the refined structure were $\phi \approx 11^\circ$ and $\theta \approx 16^\circ$, respectively, which are about twice as large as the

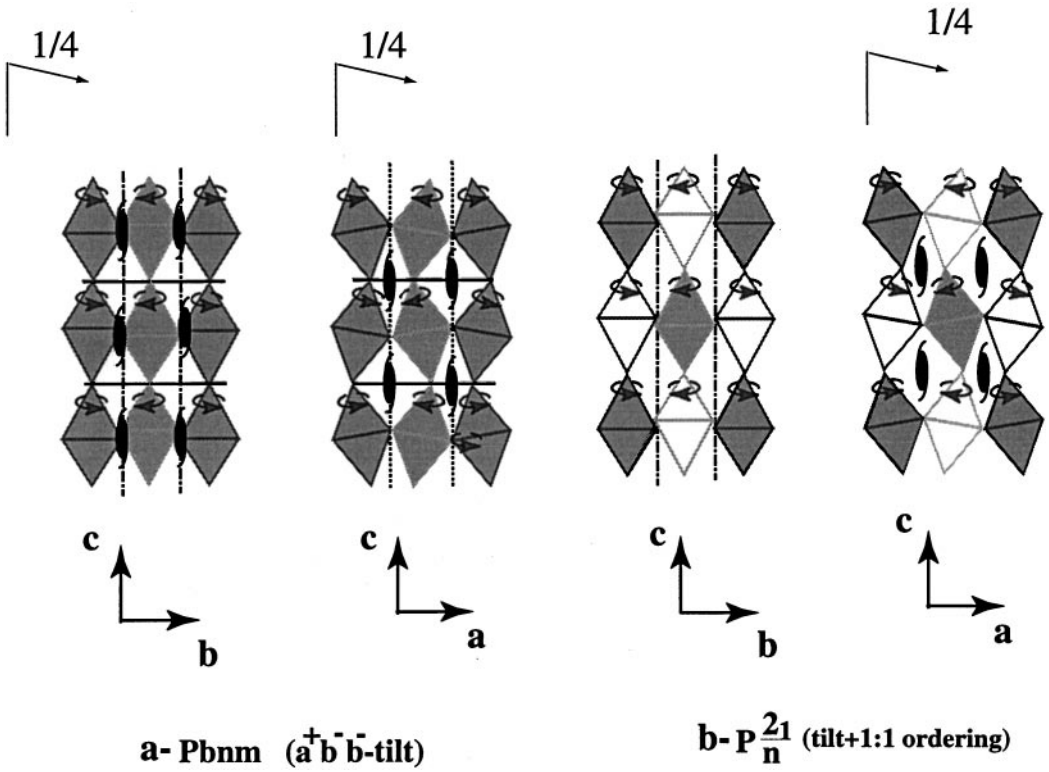

FIG. 5. Schematic $\langle 1\,1\,0\rangle_c$-projections of the perovskite-like structures with (a) $b^-b^-c^+$ octahedral tilting (*Pbnm*), (b) combination of $b^-b^-c^+$ octahedral tilting and 1:1 ordering on B-sites ($P2_1/n$). Nonequivalent Wyckoff positions are indicated by different shades. The symmetry elements are superimposed onto projections.

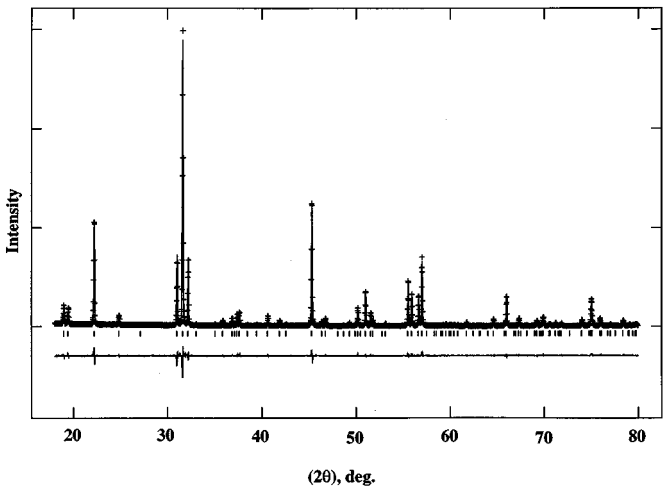

FIG. 6. (upper) Experimental (crosses) and calculated (line) XRPD patterns for the specimen A and the refined $P2_1/n$ model, correspondingly. (lower) Residual. The weighted R-factor, R_{wp}, for the calculated profile was 11.1% and the goodness of fit, χ^2, was 2.94.

corresponding angles in $CaTiO_3$ (2, 18). This significant increase in the degree of octahedral tilting is consistent with the larger deviation from unity of the tolerance factor for $Ca_4Nb_2O_9$ ($t_{CaTiO_3} = 0.973$, $t_{Ca_4Nb_2O_9} = 0.85$). The bond valence sum (19) calculated at the A = Ca site was equal to 1.88 (for the 12 oxygen ions included into the 1st coordination sphere), indicating that the A-site Ca ions are underbonded and the Ca–O bonds are stretched. Note, however, that our refined model represents the HTP structure only *approximately*, since the high-temperature structure was not completely quenchable.

Annealing of specimen A at 1500°C (10 h) followed by water-quenching resulted in significant reduction of XRPD linewidths. This effect was attributed to the strain relaxation and coarsening of the domain structure. No appreciable difference in diffraction peak widths was observed between specimens quenched from 1600 and 1650°C. These observations suggest that the displacive tilting transition(s) occurs between 1500 and 1600°C.

In summary, these results are consistent with the occurrence of two high-temperature $Ca_4Nb_2O_9$ polymorphs separated by a displacive transition at 1500–1600°C. Above the transition $Ca_4Nb_2O_9$ is either disordered or exhibits 1:1 ordering of Ca and Nb cations on the B-sites; the present results do not provide the direct evidence that would allow us to choose between the two models. Below the transition, the 1:1 ordering is combined with $b^-b^-c^+$ octahedral tilting.

TABLE 2

Lattice Parameters and Atomic Positions Derived by Rietveld Refinement ($R_{wp} = 11.1\%$, $\chi^2 = 2.94$) of the High-Temperature Structural Model with Combined 1:1 Ordering and $b^-b^-c^+$ Octahedral Tilt, Using XRPD Data from Specimen A

Lattice parameters: $a = 5.56133$ (3) Å, $b = 5.76733$ (3), $c = 9.74629$ (9) Å, $\beta = 124.81°$
Density: 4.228 g/cm^3
$Z = 4$
Space group: $P2_1/c$ (no. 14, b is the unique monoclinic axis)
Atomic positions:

Atom	x	y	z	Occupancy	Site multiplicity
Nb	0	1/2	0	1	2
Nb	1/2	0	0	1/3 = 0.3333	2
Ca	1/2	0	0	2/3 = 0.6666	2
O(1)	0.6569(8)	0.9572(5)	0.2577(6)	1	4
O(2)	0.123(1)	0.2081(6)	0.9399(7)	1	4
O(3)	0.7542(9)	0.3078(6)	0.0476(7)	1	4
Ca	0.2424(3)	0.0524(1)	0.2534(1)	1	4

Note. For convenience, both lattice parameters and atomic positions are given for the standard setting of axes with the symmetry described by the $P2_1/c$ (no. 14, setting 1) space group. The same structure can be alternatively described by the $P2_1/n$ (no. 14, setting 2) space group if nonstandard setting of axes is used. These results should be considered as approximate since the high-temperature polymorph could not be completely quenched.

Low-Temperature $Ca_4Nb_2O_9$ Structures

1. $LT_{1/4}$: $Ca_4Nb_2O_9$ phase with superlattice reflections at $1/4[111]^*_c$. A set of typical selected area electron diffraction (SAED) patterns obtained from a specimen with well-developed $1/4\langle 111\rangle^*_c$ reflections (specimen E, Table 1) is shown in Fig. 7. The reciprocal lattice consists of the lattice of the HTP_2 phase decorated by additional superlattice reflections at $1/4\langle 111\rangle^*_c$ along two of the four $\langle 111\rangle_c$ directions. The superlattice $\mathbf{k} = 1/4\langle 111\rangle^*_c$ reflections were also observable by XRPD at $2\theta \approx 9.56°$ (Fig. 8). The full set of reflections can be indexed with either orthorhombic $2\sqrt{2}a_c \times \sqrt{2}a_c \times 4a_c$ or monoclinic $\sqrt{6}a_c \times \sqrt{2}a_c \times 2\sqrt{2}a_c$, $\beta \approx 125°$ (b is the unique axis) unit cells. The orthorhombic unit cell differs slightly from that reported by Hervieu *et al.* (5) for the high-temperature phase existing above 1400°C. Indexing of the reciprocal lattice assuming the monoclinic unit cell is shown in Fig. 9.

It was observed that annealing of quenched specimens at 1000°C for a short time (10 min, Table 1) was sufficient to induce growth of the $1/4[111]^*_c$ ordered domains (Fig. 10). At lower temperatures, annealing on a scale of hours was necessary to induce growth of this phase.

The microstructure of the specimen with a fully developed $LT_{1/4}$ structure (specimen E) consists of the same type I and II domains observed in the quenched specimens. Inside these domains, smaller type III domains associated with superlattice reflections at $\mathbf{k} = 1/4[111]^*_c$ were identified (Figs. 11a, 11c, 11d). Traces of interfaces between these domains are approximately parallel to $\{100\}_c$ and $\{110\}_c$

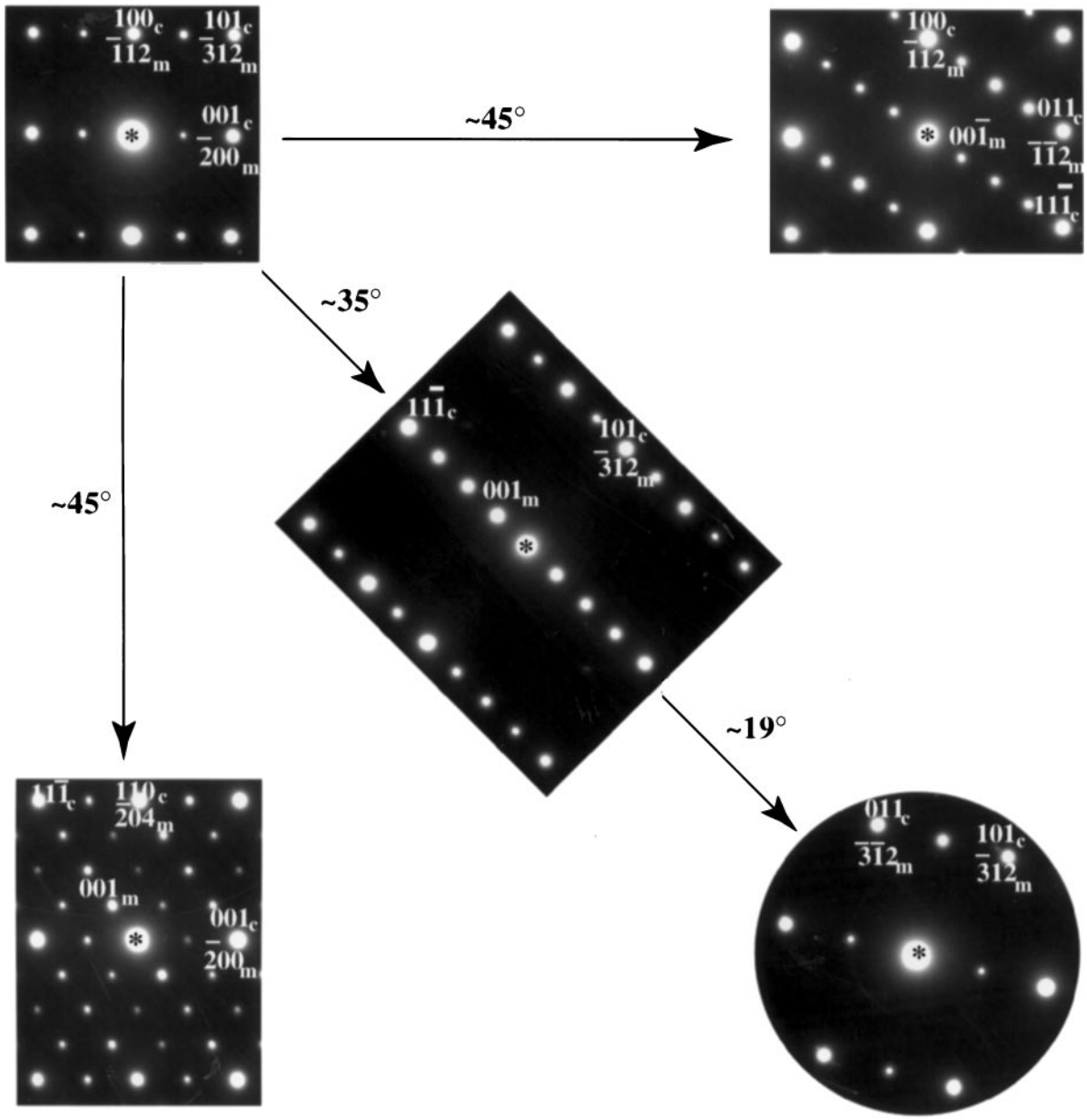

FIG. 7. Set of SAD patterns obtained from a single primary rotational domain in specimen E. The fundamental reflections are indexed using both cubic perovskite and monoclinic unit cells with lattice parameters a_c and $\sqrt{6}a_c \times \sqrt{2}a_c \times 2\sqrt{2}a_c$, $\beta = 125°$, correspondingly. In addition to reflections at $1/2[111]^*_c$ and $1/2[001]^*_c$, superlattice reflections at $\mathbf{k} = 1/4[111]^*_c$ are observed.

planes. Electron microdiffraction patterns from the two adjacent type III domains revealed appreciable variation of intensity of $1/4[111]^*_c$ and $1/4[11\bar{1}]^*_c$ reflections in each domain (Figs. 11c and 11d). Tilting experiments proved that type III domains represent rotational variants 1_m and 2_m of the monoclinic structure with $[001]^*_{m1} = 1/4[111]^*_c$ and $[00\bar{1}]^*_{m2} = 1/4[11\bar{1}]^*_c$ and lattice parameters $\sqrt{6}a_c \times \sqrt{2}a_c \times 2\sqrt{2}a_c$, $\beta = 125°$. The $(0\,k\,0) \rightarrow k = 2n$ reflection condition as observed in microdiffraction patterns is consistent with the space group $P2_1$.

Additionally, four domains (type IV) with the appearance of antiphase boundaries were identified within type III domains (Fig. 11f). Since these domains have a common reciprocal lattice, we identified them as translational antiphase domains. The interfaces between these domains show the strongest contrast when imaged with $1/4[111]^*_c$ reflections, although an appreciable residual contrast is observed in both $1/2[111]^*_c$ and $[111]^*_c$ reflections. This relatively strong residual contrast can be due to a local lattice expansion/contraction across the antiphase boundary. Quenching

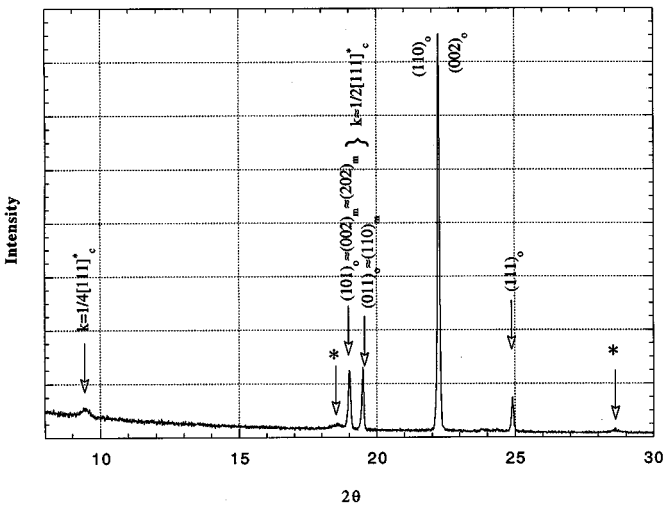

FIG. 8. Low-angle portion of the XRPD pattern from specimen C. Broad superlattice reflections associated with the "$1/4[111]_c^*$]"-phase observed in the pattern are indicated by asterisks. The subcell reflections are indexed according to the orthorhombic $\sqrt{2}a_c \times \sqrt{2}a_c \times 2a_c$ unit cell. The indexing according to the monoclinic $\sqrt{6}a_c \times \sqrt{2}a_c \times 2\sqrt{2}a_c$, $\beta = 125°$ superstructure is given for some of the subcell reflections.

experiments suggest that the transition resulting in the formation of $1/4[111]_c^*$ reflections occurs below 1400°C. SAD patterns from the quenched specimens (specimens A and B, Table 1) resulted in diffuse $1/4[111]_c^*$ reflections corresponding to small 30–50 Å ordered regions, as confirmed by both dark-field (Fig. 10a) and structural (Fig. 12) imaging. These small regions are related to each other as type III and IV domains in a fully ordered structure. Although the identification of type III rotational monoclinic domains is difficult, translational type IV domains with the antiphase shift of $R = [111]_c$ are readily observed in the structural image formed by the FFT procedure using only diffuse $1/4[111]_c^*$ reflections.

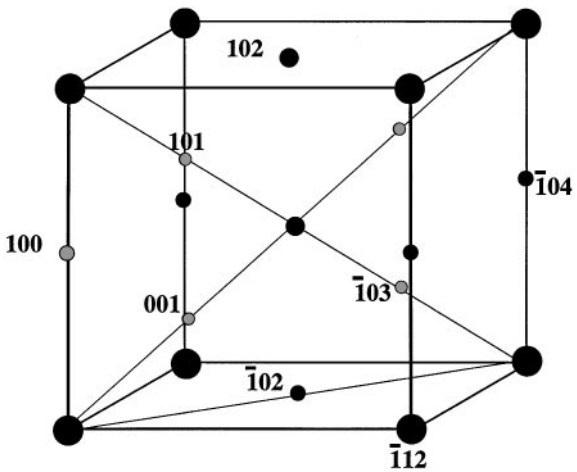

FIG. 9. Reconstructed reciprocal lattice of the structure with superlattice reflections at $1/4[1\,1\,1]_c^*$ indexed using the monoclinic unit cell with lattice parameters $\sqrt{6}a_c \times \sqrt{2}a_c \times 2\sqrt{2}a_c$, $\beta \approx 125°$.

The orientation relationship between HTP_2 and $LT_{1/4}$ structures, determined by comparison of extinctions in electron diffraction patterns from the quenched specimens, corresponds to $(100)_{HTP_2} \| (100)_{LT_{1/4}}$, $[010]_{HTP_2} \| [001]_{LT_{1/4}}$.

The dependence of the kinetics of formation of the $LT_{1/4}$ structure upon cooling rate suggests ordering rather then a displacive transition from the high-temperature phase (HTP_2). The domain size of the $LT_{1/4}$ phase was observed to increase by an order of magnitude during slow cooling from 1400 to 1200°C, which suggests that the ordering temperature is located within this temperature range.

The $\sqrt{6}a_c \times \sqrt{2}a_c \times 2\sqrt{2}a_c$ unit cell contains eight *B*-site positions, and such a structure can only be partially ordered with a $Ca(Ca_{1/3}Nb_{2/3})O_3$ stoichiometry. There are four distinct Wyckoff positions (x, y, z) in the $P2_1$ structure which describe eight *B*-sites (Fig. 13a): (1) $0\,\frac{1}{2}\,\frac{3}{8}$, (2) $0\,0\,\frac{3}{8}$, (3) $\frac{1}{2}\,0\,\frac{1}{8}$, (4) $\frac{1}{2}\,\frac{1}{2}\,\frac{3}{8}$ (no displacements of *B*-cations as compared to the 1 : 1 ordered structure were assumed). The orientation relationship between the ordering vector and the directions of tilting axes was deduced from the orientation relationship between HTP_2 and $LT_{1/4}$ structures. The contribution of any two equivalent Wyckoff positions (xyz and $\bar{x}y + \frac{1}{2}\bar{z}$), related by the twofold screw symmetry axis, to the structure factors of the (002), ($\bar{2}02$), and (110) reflections is nearly zero, assuming small displacements of *B*-cations from the ideal positions. In contrast, these reflections (Fig. 8) exhibit appreciable intensities in XRPD patterns of the $LT_{1/4}$ phase, thus suggesting the absence of twofold symmetry axes and, therefore, triclinic $P1$ symmetry for the $LT_{1/4}$ structure (Fig. 13b). Hervieu *et al.* (5) reported a similar pseudo-monoclinic unit cell for the $Ca_5Nb_3O_{12} = 4 \bullet Ca(Ca_{0.25}Nb_{0.75})O_4$ compound synthesized in argon (the Nb charge must be +4.67 to satisfy the electroneutrality condition). They proposed that the $Ca_5Nb_3O_{12}$ structure exhibits 3:1 ordering of Ca and Nb cations on *B*-sites.

Microdiffraction patterns obtained along the [010] axis of the $LT_{1/4}$ structure show that the intensity of the $(\bar{1}01)_{tr} = 1/4(11\bar{1})_c$ reflection is significantly smaller than that of the $(001)_{tr} = 1/4(111)_c$ reflection (Figs. 11d and 11e). Tilting experiments demonstrated that the intensity of $(100)_{tr}$ reflection remains zero in the transformed $P1$ structure. All ($\bar{1}01$), (001), and (100) superlattice reflections arise primarily due to additional redistribution of Ca and Nb cations on the *B* sites as compared to the 1 : 1 ordered HTP_2 structure. The contributions of eight nonequivalent *B*-sites (Fig. 13b) to the structure factors of (001), (101), (100), and ($\bar{2}02$) reflections are summarized in Table 3 along with the qualitative estimate of intensities experimentally observed.

2. $LT_{1/6}$: $Ca_4Nb_2O_9$ polymorph with superlattice reflections at $\mathbf{k} = 1/6[1\,1\,1]_c^*$. Prolonged annealing at $T \leq$

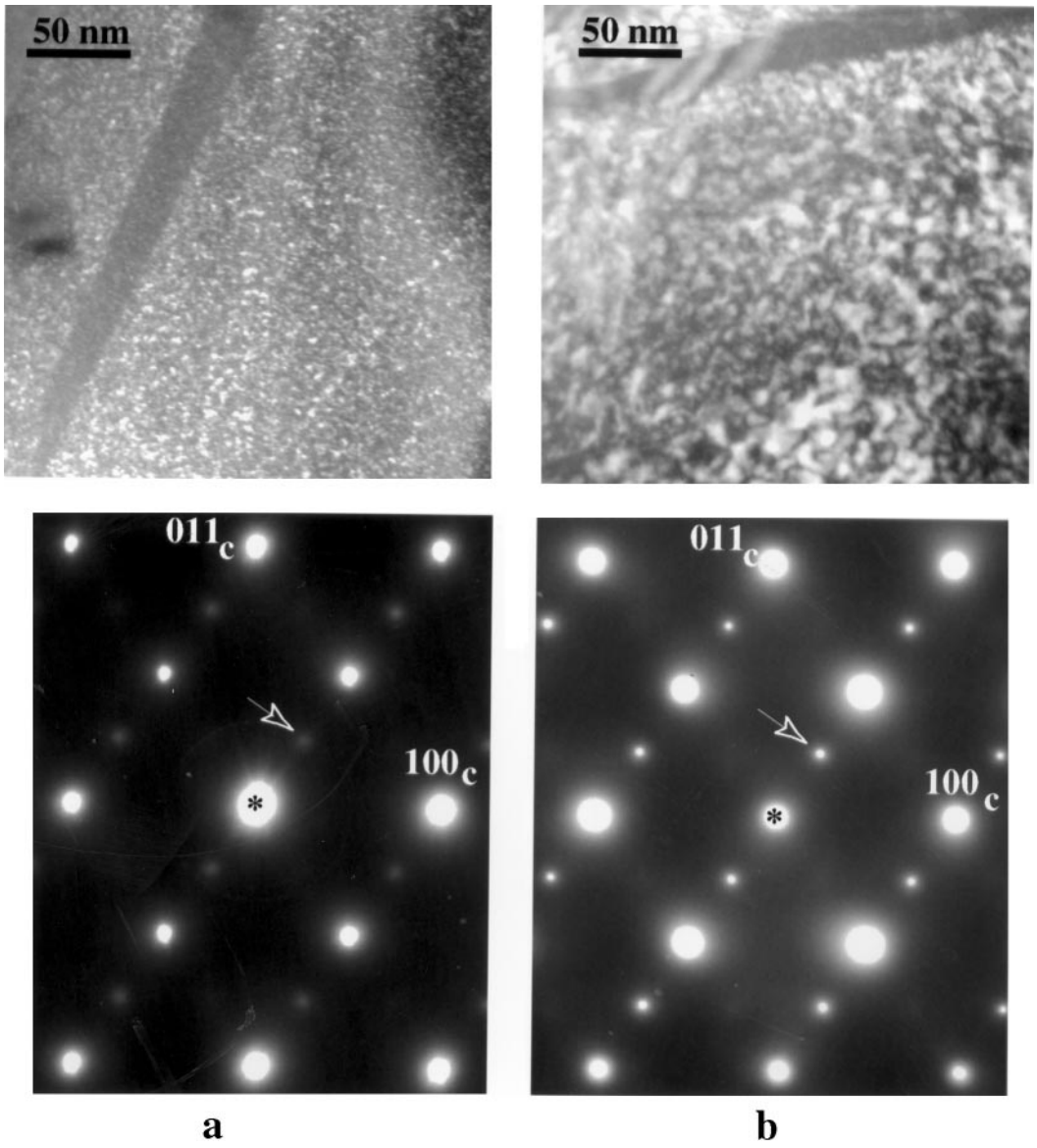

FIG. 10. Dark field images and the corresponding SAD patterns from the single primary domain in the specimens A (a) and C (b), respectively. Both dark field images were recorded with $3/4[111]^*_c$ reflections close to two-beam conditions near the $\langle 110 \rangle_c$ zone axis orientation. The increase in the size of domains corresponding to the $1/4[111]^*_c$-type superlattice reflections is observed after annealing of specimen A at 1000°C for 10 min.

1400°C resulted in the transformation of the $LT_{1/4}$ phase to a "$LT_{1/6}$" phase with superlattice reflections at $1/6[1\,1\,1]^*_c$ (specimens D and H, Table 1). The transformation occurs by precipitation and growth of the $LT_{1/6}$ phase, e.g., nuclei of the $LT_{1/6}$ phase formed in specimen E during continuous cooling from 1400 to 1200°C (in 9 min), followed by air quenching. The transformation was completed during subsequent annealing at 1300°C for 1 h (specimen F, Table 1). Prolonged annealing at 1000°C (66 h) also resulted in a phase transition from $LT_{1/4}$ to $LT_{1/6}$. These observations indicate that the $LT_{1/6}$ phase is stable below 1400°C.

A typical set of SAD patterns from this phase is shown in Fig. 14. The XPRD pattern reveals a characteristic superlattice reflection at $2\theta \approx 12°$, which corresponds to $\mathbf{k} = 1/3[111]^*_c$. Both SAED and XRPD patterns are similar to those presented in reference (5) and can be indexed using a monoclinic unit cell with approximate lattice parameters $a_m = a_c\sqrt{6}$, $b_m = a_c\sqrt{2}$, $c_m = 3a_c\sqrt{2}$, $\beta \approx 125°$. The refined values of the lattice parameters from XRPD are $a = 9.8159(1)$ Å, $b = 5.53628(5)$ Å, $c = 17.35016(16)$ Å, and $\beta = 125.5007(4)°$. The symmetry of this phase as determined from the reflection conditions corresponds to the $P2_1/c$

space group, which also agrees with that proposed by Hervieu *et al.* (5).

Formation of the $LT_{1/6}$ phase occurs by precipitation inside $LT_{1/4}$ grains, as was captured in specimen E (Fig. 15). The precipitates have a platelike shape with the plate face normal to the $\mathbf{k} = 1/6[111]^*_c$. Only two ($\mathbf{k}_1 = 1/6[111]^*$ and $\mathbf{k}_2 = 1/6[11\bar{1}]^*$) variants of the $LT_{1/6}$ phase typically form in a single domain of the $LT_{1/4}$ phase. The orientation relationship between the matrix and precipitate lattices typically observed corresponded to $[010]_{matrix} \| [010]_{precip}$, $(100)_{matrix} \| (100)_{precip}$ (monoclinic indexes).

Because the formation of $LT_{1/6}$ is preceded by the $HTP_1 \rightarrow HTP_2$ displacive phase transition occurring between high-temperature phases, the same rotational type I and type II domains and associated interdomain boundaries (Fig. 4) are preserved in the fully developed $LT_{1/6}$ phase. Inside these primary domains, two types of secondary domains are observed. Domains of the first type are rotational domains (II^1_1, II^2_1, II^1_2, II^2_2 in Fig. 16) with traces of interdomain boundaries approximately parallel to the $(001)_c$ planes. Microdiffraction patterns in both $[100]_c$ and $[110]_c$ orientations from the adjacent domains of this type confirm

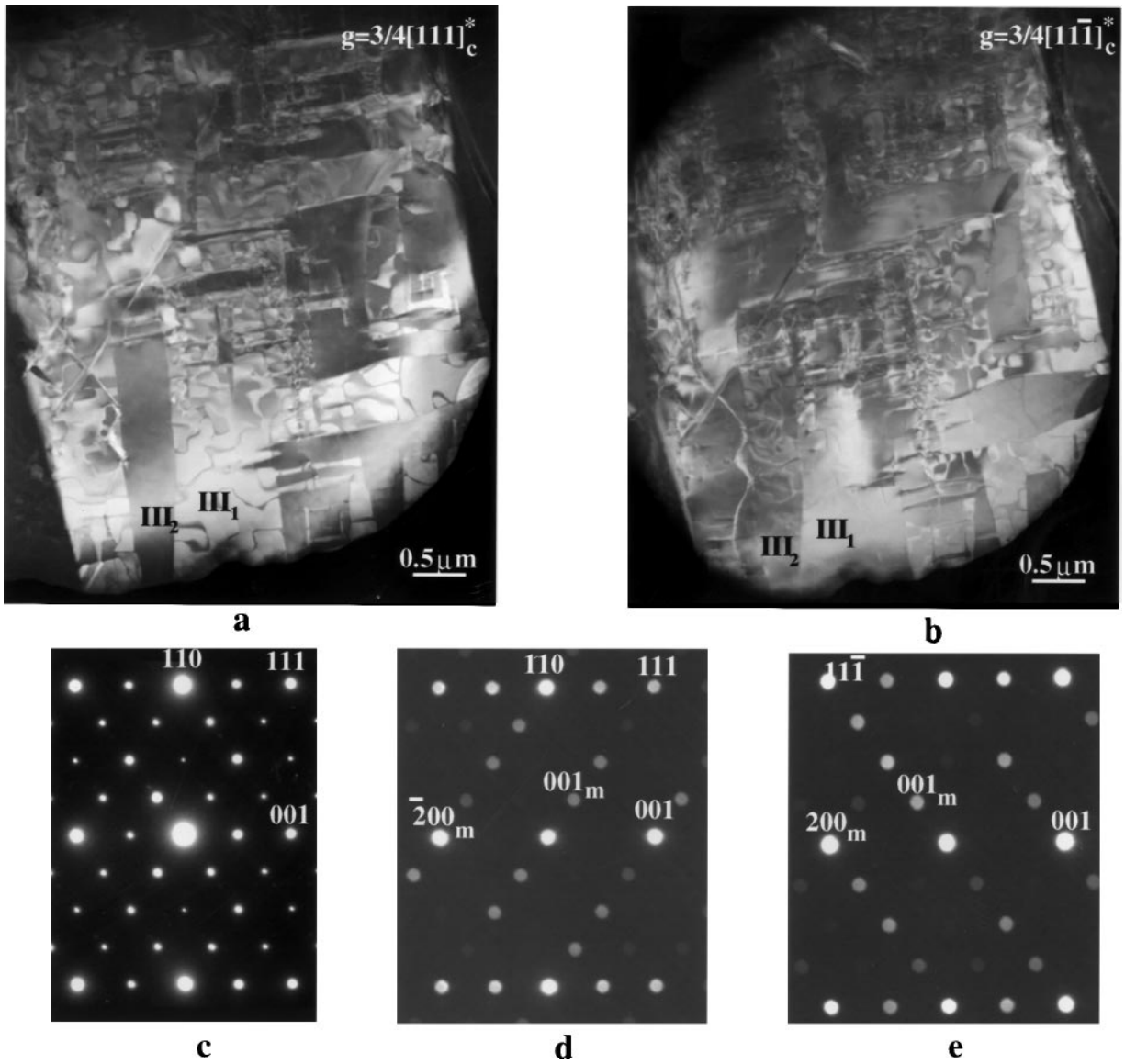

FIG. 11. Dark field images obtained close to the two-beam conditions from a single type II rotational domain in (a) $3/4[111]^*_c$ and (b) $3/4[11\bar{1}]^*_c$ reflections. Twin related domains III_1 and III_2 are indicated in the images. c) SAD from a type II domain. (d, e) Microdiffraction patterns from III_1 and III_2 domains, correspondingly. (f) Enlarged image of the III_1 domain showing the presence of translational interlocked domains, indicated as IV_1, IV_2, and IV_3.

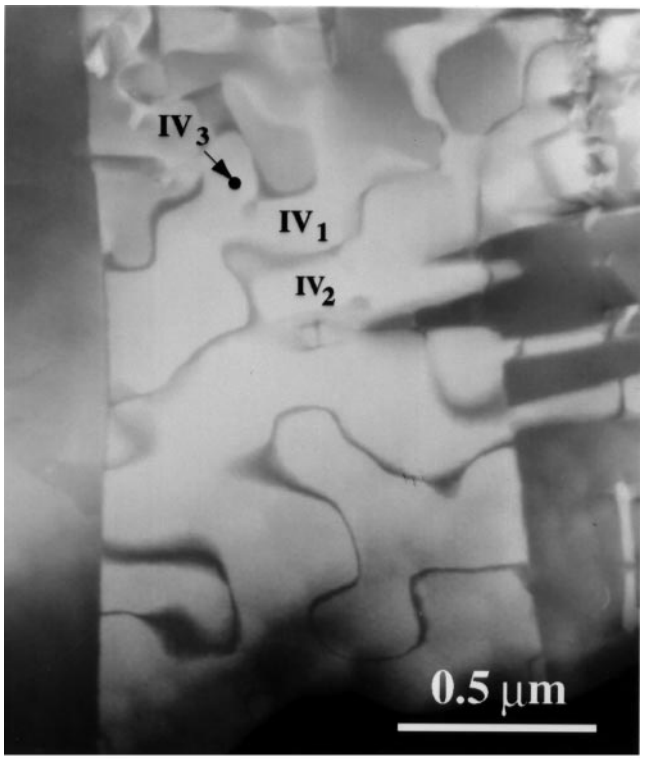

f

FIG. 11—*Continued*

that they represent twin-related monoclinic variants of the $P2_1/c$ structure. This observation implies that the primary domains are inherited from the initial state and the secondary domains are induced by impingement of precipitates with a monoclinic $P2_1/c$ structure. Each monoclinic variant has a high density of faceted translational interfaces visible only in $1/6[111]_c^*$-type superlattice reflections (Fig. 17). These boundaries are predominantly parallel to $\{111\}_c$ planes (with the ordering vector normal to the plane). Other, short facets reside on $\{001\}_c$ planes. Three translational variants were identified in the dark-field images (Fig. 17), which is consistent with 2 : 1 ordering of Ca and Nb cations on $\{111\}_c$ planes (ordering vector $1/3[111]_c^*$), as proposed by Hervieu *et al.* (5). Similarly to the rotational domains, formation of antiphase boundaries is attributed to the impingement of growing precipitates.

Heating the $LT_{1/6}$ phase above 1400°C followed by water quenching reproduced small $LT_{1/4}$ domains dispersed in a matrix of untransformed HTP_2 phase. However, additional planar defects *not* observed in specimens A, B, or E were detected in the reheated specimens (Fig. 18). The defects exhibit contrast similar to that from antiphase boundaries and are faceted predominantly along $(111)_c$ planes. The defects exhibit the strongest contrast when imaged with $1/2\langle 111\rangle_c^*$ reflections; furthermore, the normals to *all* the long facets in the particular primary domain are parallel to the same $[111]_c$ direction. These planar defects can be interpreted as antiphase boundaries formed

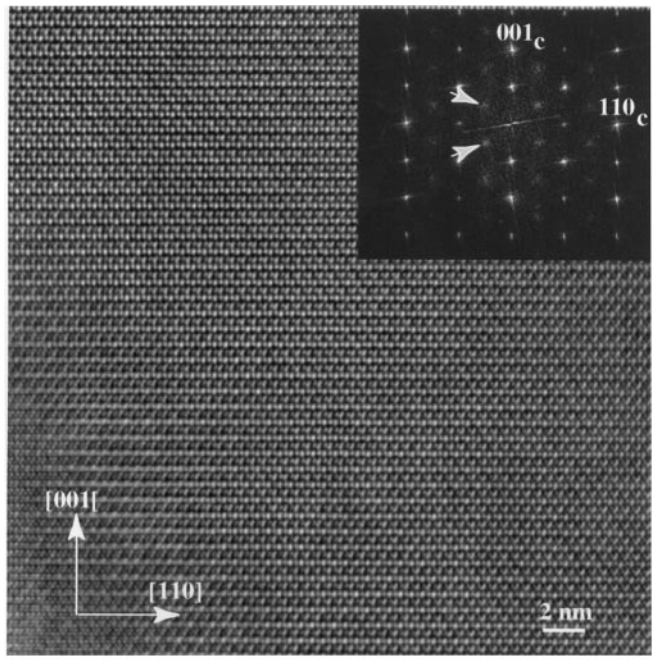

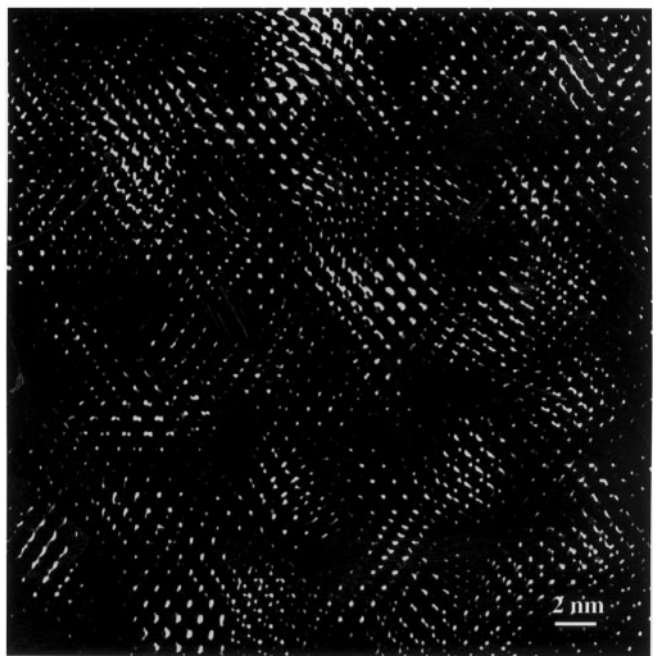

FIG. 12. (top) Structural image of a single primary domain in the $\langle 110\rangle_c$ orientation parallel to the unique monoclinic axis of the structure with superlattice reflections at $\mathbf{k} = 1/4[111]_c^*$. The image was obtained from the specimen water quenched from 1600°C (specimen A). The FFT of this image with diffuse superlattice reflections at $1/4[111]_c^*$ is shown as the insert. (bottom) The same image FFT filtered using $1/4[111]_c^*$ reflections. The presence of both ordered domains and the disordered matrix is evident.

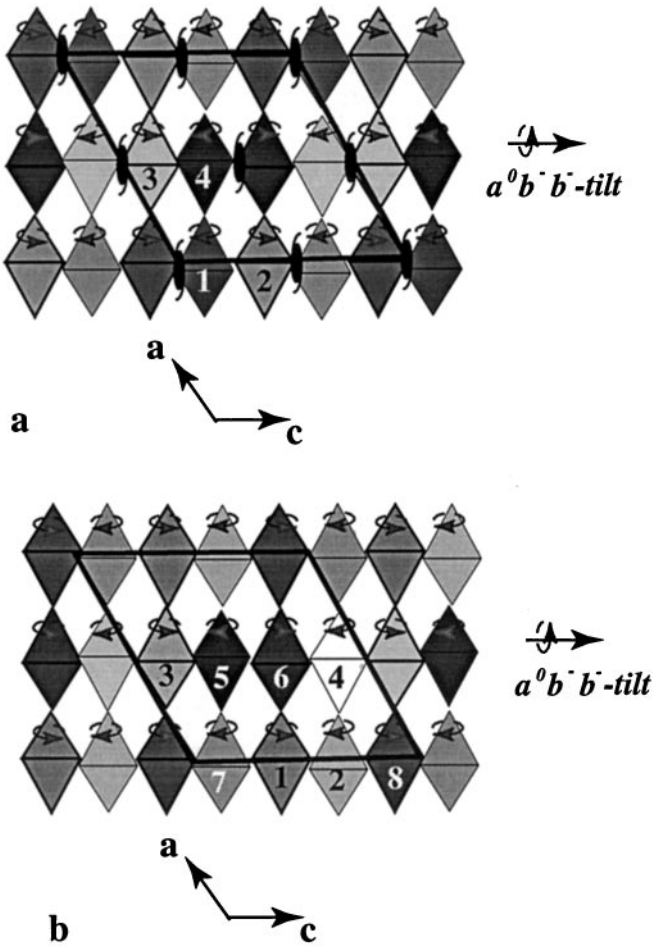

FIG. 13. Schematic $\langle 110\rangle_c$-projections of the perovskite-related structure with a combination of $a^+b^-b^-$ octahedral tilting and $\mathbf{k} = 1/4[111]^*_c$ ordering on *B*-sites. (a) Structure with $P2_1$ monoclinic symmetry. (b) Structure with *P*1 triclinic symmetry. Nonequivalent Wyckoff positions are indicated by different shades and numbers, and the symmetry elements are superimposed onto projections.

from impingement of 1:1 ordered high-temperature-phase precipitates growing in antiphase. Two translational variants were identified in the dark-field images consistent with a $\mathbf{k} = 1/2[111]^*_c$ ordering vector operating in the 1:1 ordered structure. These antiphase boundaries result in streaks of diffuse intensity parallel to the $[111]_c$ direction in the corresponding SAD pattern. The streaks pass *only* through those superlattice reflections ($1/2[111]^*_c$) which are expected for both cation ordering and octahedral tilting, while the superlattice reflections at $1/2[221]^*_c$, which arise solely due to octahedral tilting, do not exhibit streaks. These observations suggest that the antiphase boundaries are associated with 1:1 ordering of cations on the *B*-sites, supporting the results of Rietveld refinement of HTP_2 phase.

DISCUSSION

Symmetry Relations between the Observed Structures

Structural information on four $Ca_4Nb_2O_9$ polymorphs identified in the present study is summarized in Table 4. All these polymorphs have perovskite-related structures that can be derived from the aristotypic $Pm\bar{3}m$ perovskite arrangement by structural changes that result in continuous reductions in symmetry. The symmetry group/subgroup relations for the tilting transitions in simple perovskites and those for the common arrangements of *B*-cations have been discussed in the literature (20–22). The symmetry tree connecting the $Pm\bar{3}m$ structure with the structures of the four $Ca_4Nb_2O_9$ polymorphs is given in Fig. 19; the octahedral tilting systems and the types of *B*-cation ordering responsible for each symmetry reduction are included.

The structure of the $LT_{1/6}$ phase can be described as a combination of 2:1 ordering of Ca and Nb cations on the *B*-sites of the perovskite structure plus a $b^-b^-c^+$ octahedral tilting system. The cation ordering pattern corresponds to Ca (B') and Nb (B'') ions arranged on $\{111\}_c$ planes with the sequence $\{B'B''B''\}$ (23). In the absence of octahedral tilting, the ordering results in a trigonal $P\bar{3}m1$ structure (lattice parameters $a = \sqrt{2}a_c$, $c = \sqrt{3}a_c$) with superlattice reflections at $\mathbf{k} = 1/3[111]^*_c$ (Fig. 19). The symmetry of the structure that results from the combination of 2:1 ordering and $b^-b^-c^+$ tilting can be obtained from the intersection of the space groups $P\bar{3}m1$ and *Pbnm*. This results in two distinct monoclinic structures with common unit cells ($a_m = a_c\sqrt{6}$, $b_m = a_c\sqrt{2}$, $c_m = 3a_c\sqrt{2}$, and $\beta \approx 125°$), but different $P1(2_1/c)1$ or $P1(2_1/a)1$ space groups (Fig. 20) with different orientations of the tilting axes. Both these space groups are

TABLE 3

Contribution of *B*-sites into structure factors of (101), (001), and (100) Superlattice Reflections of the Triclinic *P*1 Metastable Structure

hkl	F_{hkl}	Relative intensity
(001)	Re: $-f_1-f_2+f_3+f_4-f_5-f_6+f_7+f_8$	strong
	Im: $f_1-f_2+f_3-f_4+f_5-f_6+f_7-f_8$	
($\bar{1}$01)	Re: $-f_1-f_2-f_3-f_4+f_5+f_6+f_7+f_8$	weak, ≈ 0
	Im: $f_1-f_2-f_3+f_4-f_5+f_6+f_7-f_8$	
(100)	Re: $f_1+f_2-f_3-f_4-f_5-f_6+f_7+f_8$	zero
	Im: zero	
($\bar{2}$02)	Re: zero	strong
	Im: $-f_1+f_2+f_3-f_4-f_5+f_6+f_7-f_8$	

Note. f_1 through f_8 correspond to the scattering factors of eight nonequivalent Wyckoff positions describing *B*-sites (1) 0 0 $\frac{3}{8}$, (2) 0 $\frac{1}{2}$ $\frac{5}{8}$, (3) $\frac{1}{2}$ 0 $\frac{1}{8}$, (4) $\frac{1}{2}$ $\frac{1}{2}$ $\frac{7}{8}$, (5) $\frac{1}{2}$ $\frac{1}{2}$ $\frac{3}{8}$, (6) $\frac{1}{2}$ 0 $\frac{5}{8}$, (7) 0 $\frac{1}{2}$ $\frac{1}{8}$, (8) 0 0 $\frac{7}{8}$. "Re" and "Im" refer to the real and the imaginary components of the structure factor, correspondingly.

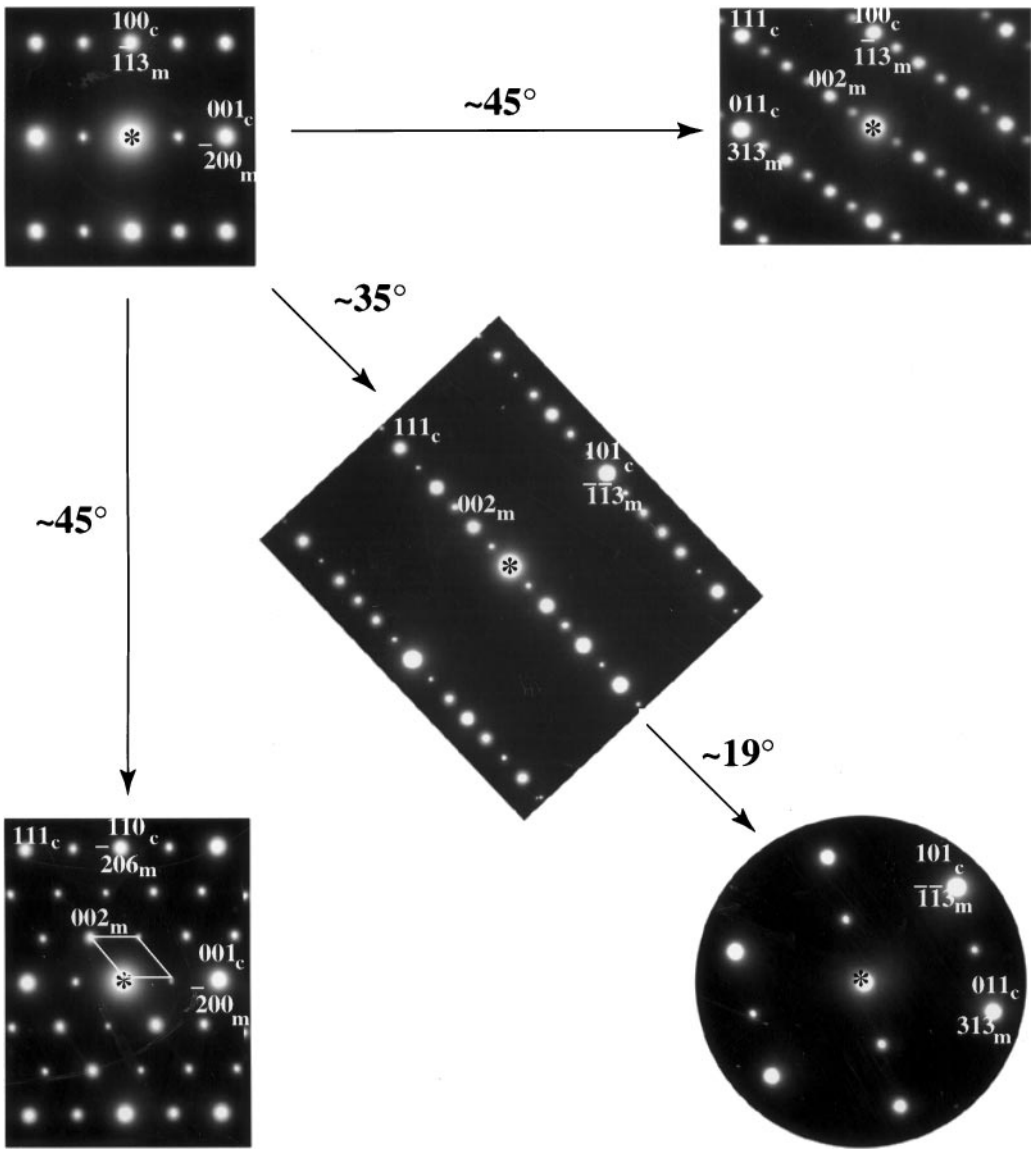

FIG. 14. Set of SAD patterns from the single primary domain in the specimen annealed at 1300°C. The fundamental reflections are indexed using the cubic perovskite unit cell with lattice parameter a_c. Superlattice reflections are indexed according to the monoclinic unit cell with lattice parameters $a_c\sqrt{6} \times a_c\sqrt{2} \times 3a_c\sqrt{2}$, $\beta \approx 125°$.

subgroups of *Pbnm*. The extinctions observed experimentally for the $LT_{1/6}$ $Ca_4Nb_2O_9$ phase are consistent with the $P1(2_1/c)1$ space group.

Similarly, the crystal structure of $LT_{1/4}$ can be described as a combination of $b^-b^-c^+$ octahedral tilting with $\mathbf{k} = 1/4[111]^*_c$ ordering of Ca/Nb cations on the (B-sites. Algebraic analysis of the structure factors for the $(\bar{1}01)$, (001), and $(\bar{2}02)$ reflections (Table 3) suggests that $c_1 + c_4 \approx c_5 + c_8$, $c_2 + c_3 \approx c_6 + c_7$, and $c_2 + c_3 \neq c_1 + c_4$, where c_i is the composition of the i site. Thus, a number of possible cation ordering schemes can be generated. For example, a 3:1 ordering is illustrated schematically in Fig. 21, wherein sites (3) and (7) are occupied exclusively by Ca cations, and all other sites are occupied by a disordered mixture of the Nb and the remaining Ca cations. Rietveld refinement of the possible models using X-ray powder diffraction is now in progress. The untilted 3:1 ordered structure with ordering vector equal to $\mathbf{k} = 1/4[111]^*_c$ would exhibit Pm monoclinic symmetry with lattice parameters $a_m = a_c\sqrt{6}$, $b_m = a_c\sqrt{2}$, $c_m = 2a_c\sqrt{2}$, and $\beta \approx 125°$. The intersection of the *Pm* space group with the *Pbnm* space group representing symmetry of the $a^+b^-b^-$ tilted octahedral framework results in a triclinic *P*1 structure. To the best of our knowledge the existence of cation ordering

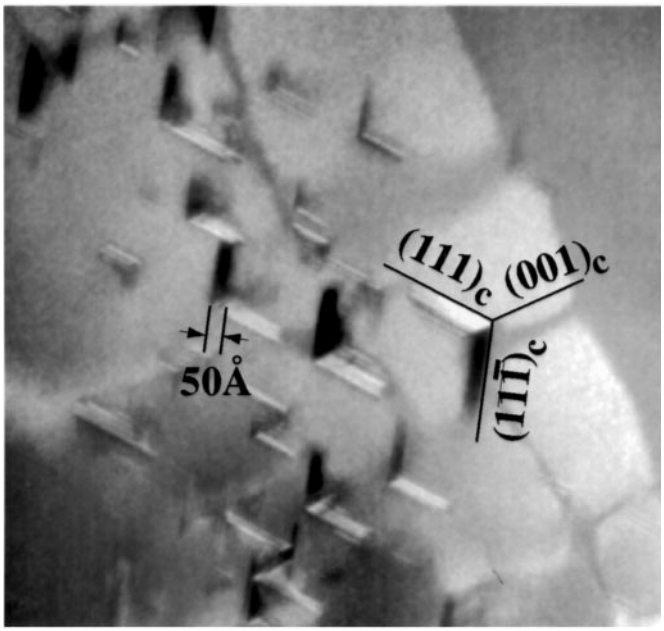

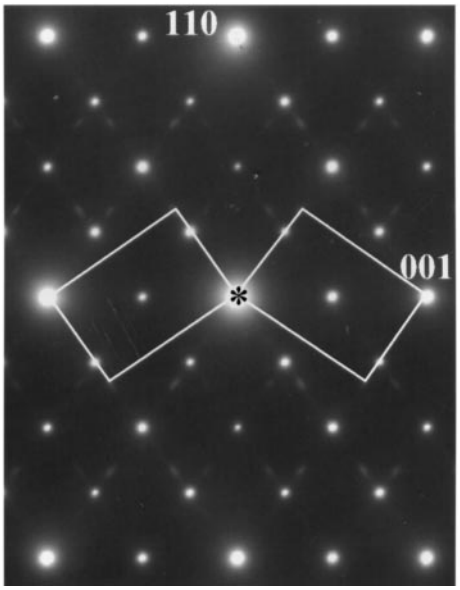

FIG. 15. (top) Dark field image in both $1/3[111]^*_c$ and $1/4[111]^*_c$ reflections recorded near the $\langle 110\rangle_c$ zone axis orientation, parallel to the unique monoclinic axes of the corresponding structures. Precipitates of two, twin related, variants with $\mathbf{k}_1 = 1/3[111]^*_c$ and $\mathbf{k}_2 = 1/3[11\bar{1}]^*_c$ are observed in a single domain of the $LT_{1/4}$ structure. (bottom) Corresponding $\langle 110\rangle_c$-SAD pattern showing superlattice reflections of both the matrix and the precipitates.

with the ordering vector $\mathbf{k} = 1/4[111]^*_c$ has never been reported for the untilted $A(B'_{1/3}B''_{2/3})O_3$ structures; that is, it may be that the presence of octahedral tilting induces $1/4[111]^*_c$ ordering as the temperature is reduced. The $LT_{1/4}$ structure apparently becomes the stable intermediate temperature polymorph (approximately in the temperature range 1400–1500°C) at a nonstoichiometric composition of 79% CaO: 21% Nb_2O_5 (24).

Analysis of symmetry relations indicates that the $P2_1/n$ (HTP_2) structure formally can be derived from the HTP_1 either by a sequence of continuous tilting transitions $a^0a^0a^0 \rightarrow a^0a^0c^+ \rightarrow b^-b^-c^+$ or by a sequence $a^0a^0a^0 \rightarrow a^0a^0c^- \rightarrow a^0b^-c^+ \rightarrow b^-b^-c^+$, which involves discontinuous $a^0b^-c^+ \rightarrow b^-b^-c^+$ (or direct $a^0a^0c^- \rightarrow b^-b^-c^+$) transition (Fig. 19). The $P1$ ($LT_{1/4}$) and the $P2_1/c$ ($LT_{1/6}$) space groups are *not* subgroups of $P2_1/n$ (HTP_2); therefore, both the $HTP2 \rightarrow LT_{1/4}$ and the $HTP_2 \rightarrow LT_{1/6}$ phase transformations must be first-order transitions with a change in the direction of the unique monoclinic axis. The $LT_{1/4} \rightarrow LT_{1/6}$ transformation also must be a first-order transition, since $P2_1/c$ ($LT_{1/6}$) is not a subgroup of $P1$ ($LT_{1/4}$), which is consistent with the precipitate-type formation of $LT_{1/6}$.

The results obtained here indicate that the temperature of the $HTP_2 \rightarrow LT_{1/4}$-phase transformation is lower than that

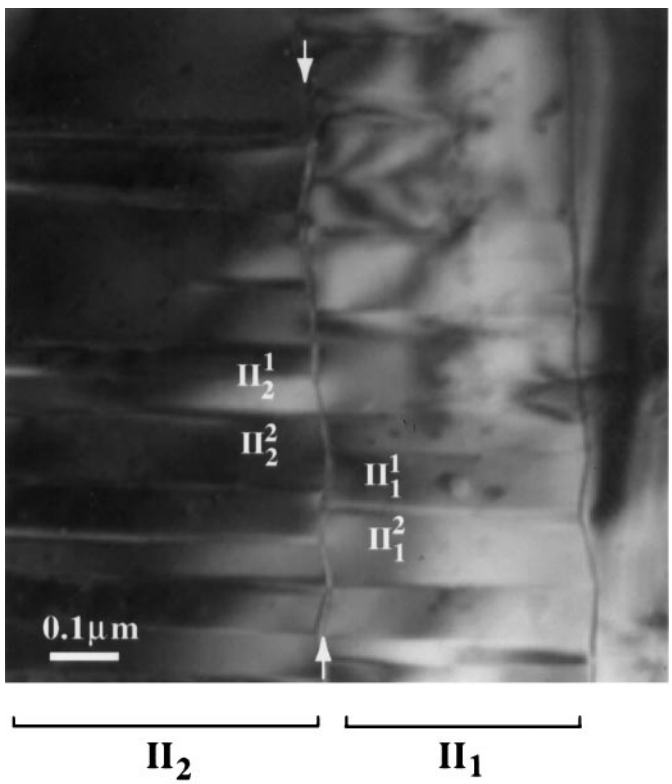

FIG. 16. Bright field image of the domain structure in the specimen annealed at 1300°C (specimen F). The image shows two twin-related type II domains, indicated as II_1 and II_2, similar to those shown in Figs. 4a and 4b. The interface between these domains (indicated by arrows) is approximately parallel to the $\{001\}_c$ plane. Inside type II domains, additional rotational domains are observed with the interdomain boundaries also approximately parallel to $\{001\}_c$, but normal to the II_1/II_2 interface. Electron microdiffraction patterns from these secondary domains confirmed that they represent twin related monoclinic variants of the $LT_{1/6}$ structure.

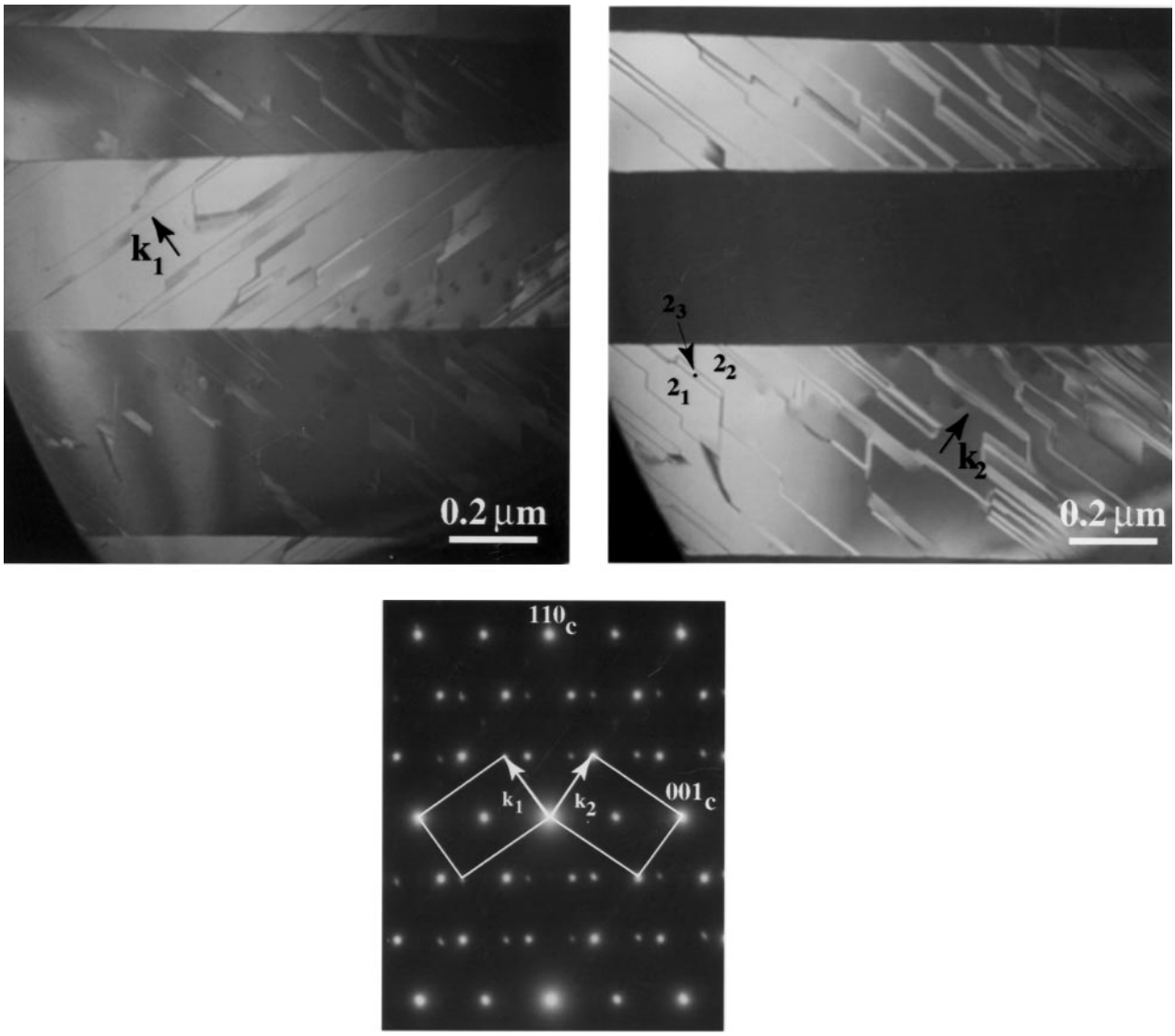

FIG. 17. Dark field images of the twin-related monoclinic variants of the $LT_{1/6}$ structure with the parallel unique monoclinic axes obtained with (top left) $\mathbf{k}_1 = 2/3[111]^*_c = [002]^*_{m1}$ and (top right) $\mathbf{k}_2 = 2/3[11\bar{1}]^*_c = [002]^*_{m2}$ reflections. Three translational variants separated by antiphase boundaries are observed in each of the rotational domains. (bottom) Corresponding SAD pattern.

of the $HTP_2 \rightarrow LT_{1/6}$ transition; nevertheless, the metastable $LT_{1/4}$ structure forms prior to the stable $LT_{1/6}$ phase. This observation is consistent with the analysis of cation configurations which showed that the $HTP_2 \rightarrow LT_{1/6}$ transition requires significantly larger rearrangements of Ca and Nb cations than the $HTP_2 \rightarrow LT_{1/4}$ transition; hence, the $HTP_2 \rightarrow LT_{1/6}$ transition is characterized by slower kinetics.

Microstructural Hierarchy

The $HTP_1 \rightarrow HTP_2$ transformation path starting at either the $Pm\bar{3}m$ disordered or the $Fm\bar{3}m$ 1 : 1-ordered structure formally implies the formation of orientational crystallographic variants according to the sequence of continuous cubic (**C**) $\rightarrow$ tetragonal (**T**) ($Fm\bar{3}m \rightarrow I4/mmm$), T $\rightarrow$ orthorhombic (**O**) ($I4/mmm \rightarrow P4/mnc \rightarrow Pnnm$), and **O** $\rightarrow$ monoclinic (**M**) ($Pnnm \rightarrow P2_1/n$) symmetry reductions. Lattice deformations associated with each of these symmetry changes generate spontaneous strain, and the strain tensors in different orientational variants are related by the symmetry operations lost during the transition. The strain energy of a system is minimized if interdomain boundaries are oriented to preserve a strain compatibility between two adjacent domains, representing different orientational variants of the transformed structure. The permissible

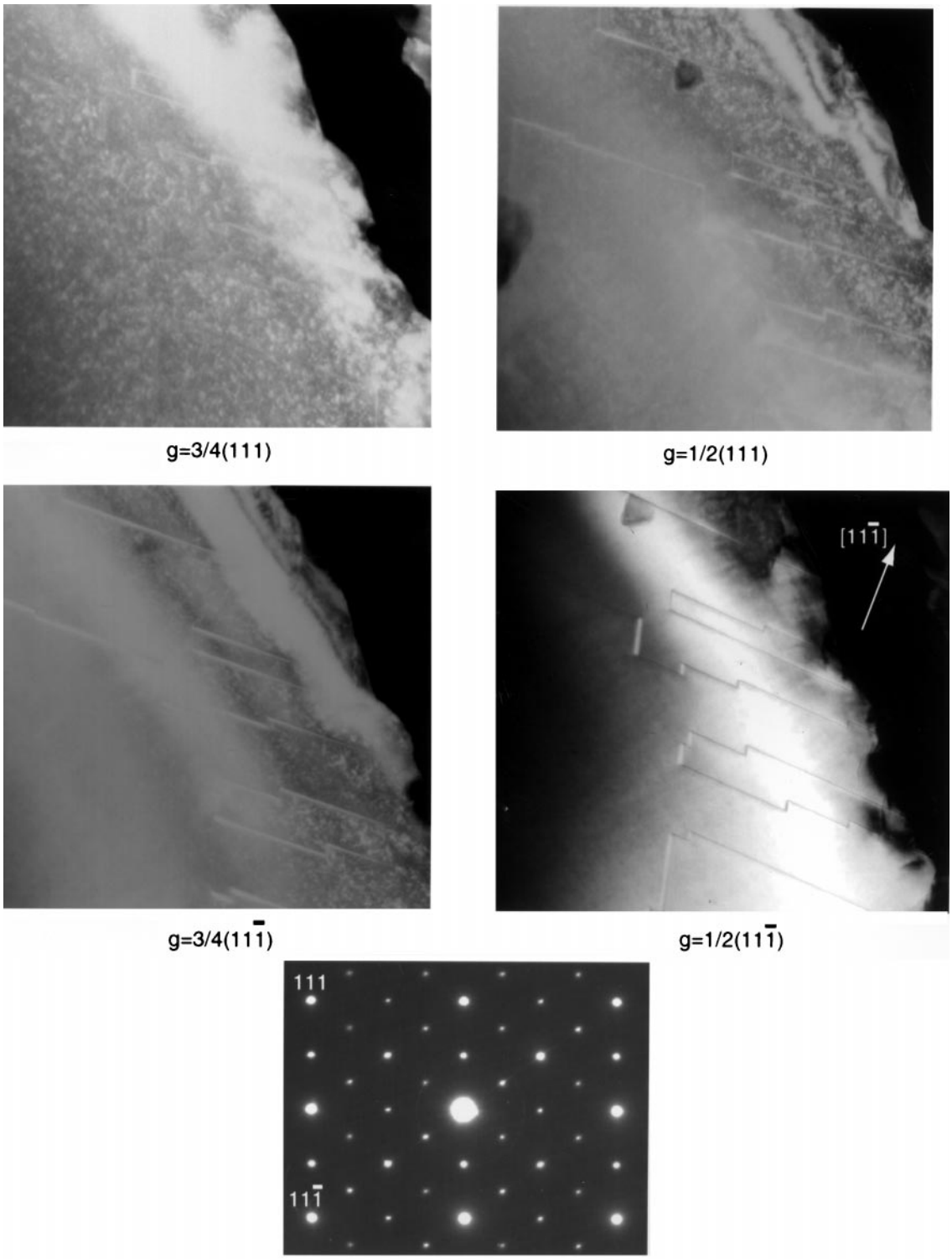

FIG. 18. (top four images) Dark field images in $\mathbf{g} = 3/4\langle 111\rangle_c^*$ and $\mathbf{g} = 1/2\langle 111\rangle_c^*$ reflections strongly excited near the $\langle 110\rangle_c$ zone axis orientation (specimen G). Two translational variants separated by antiphase boundaries, faceted predominantly on the $(11\bar{1})$ plane, are observed in the image. These interfaces show strong contrast only when imaged in $\mathbf{g} = 1/2\,[11\bar{1}]_c^*$ reflection. (bottom image) SAD pattern from the same area. Diffuse streaks of intensity parallel to the $[11\bar{1}]$ direction are observed in the pattern.

TABLE 4
Structural Information on $Ca_4Nb_2O_9$ Polymorphs

Phase	Space group	Lattice parameters	Ordering	Tilting
HTP_1	$Pm\bar{3}m$ or $Fm\bar{3}m$	a_c	disordered	none
		$2a_c$	1:1	
HTP_2	$P2_1/n$	$\sqrt{2}a_c \times \sqrt{2}a_c \times 2a_c$	1:1	$b^-b^-c^+$
$LT_{1/4}$	$P1$	$\sqrt{6}a_c \times \sqrt{2}a_c \times 2\sqrt{2}a_c$, $\alpha \approx \gamma \approx 90°$, $\beta \approx 125°$	$1/4[111]_c^*$	$b^-b^-c^+$
$LT_{1/6}$	$P2_1/c$	$\sqrt{6}a_c \times \sqrt{2}a_c \times 3\sqrt{2}a_c$, $\beta \approx 125°$	2:1	$b^-b^-c^+$

orientations of such strain-free interfaces has been tabulated for all possible point-group symmetry reductions (25). The $\mathbf{C} \rightarrow \mathbf{T}$ transition is expected to produce six rotational domains separated by strain-free interfaces parallel to $\{110\}_c$ planes, while the subsequent $\mathbf{T} \rightarrow \mathbf{O}$ transition will induce additional subdivision of domains, with strain-free interdomain interfaces always parallel to $\{001\}_c$ planes. Finally, the $\mathbf{O} \rightarrow \mathbf{M}$ symmetry reduction subdivides orthorhombic domains onto monoclinic domains with the common unique axes separated by strain-free interfaces parallel to either $\{110\}_c$ or $\{001\}_c$ planes. Similar types of domains, but without well-defined spatial hierarchy, are expected for the sequences which involve discontinuous $C2/c$ $(b^0b^-c^+) \rightarrow P2_1/n$ $(b^-b^-c^+)$ or $I4/m$ $(a^0a^0c^-) \rightarrow P2_1/n$ $(b^-b^-c^+)$ transitions.

The types of domains and their spatial hierarchy observed in the quenched specimens (Fig. 4) in general are consistent with those expected from the formal symmetry

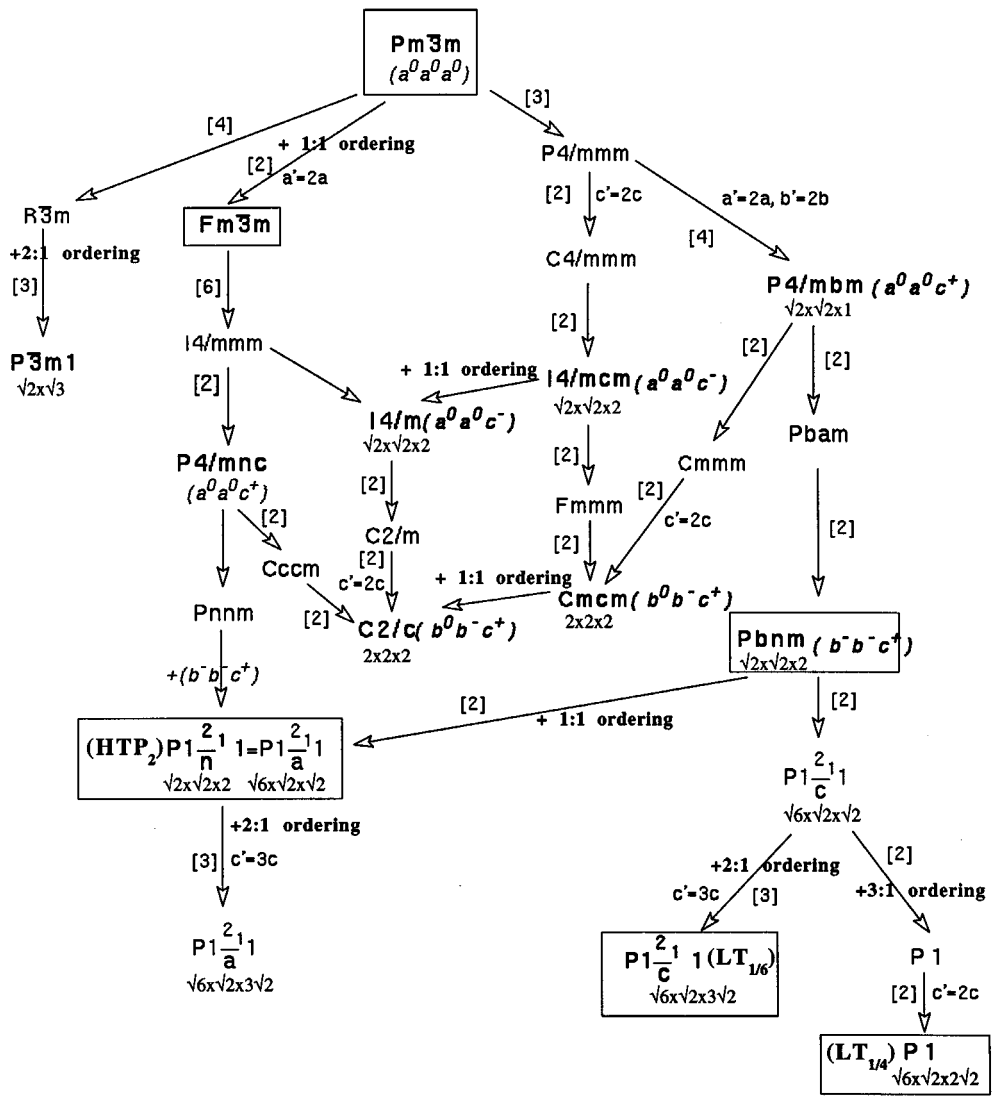

FIG. 19. Sequences of maximal symmetry group/subgroup relations between the ideal cubic perovskite structures and structures with combinations of the most common tilt systems ($a^0a^0c^+$, $a^0b^-b^-$, $a^+b^-b^-$, $a^-a^-a^-$) and ordered arrangements of *B*-cations (1:1, 2:1, and "$1/4[1\,1\,1]_c^*$" orderings). The numbers in brackets refer to the number of crystallographic variants resulting from each minimal symmetry reduction.

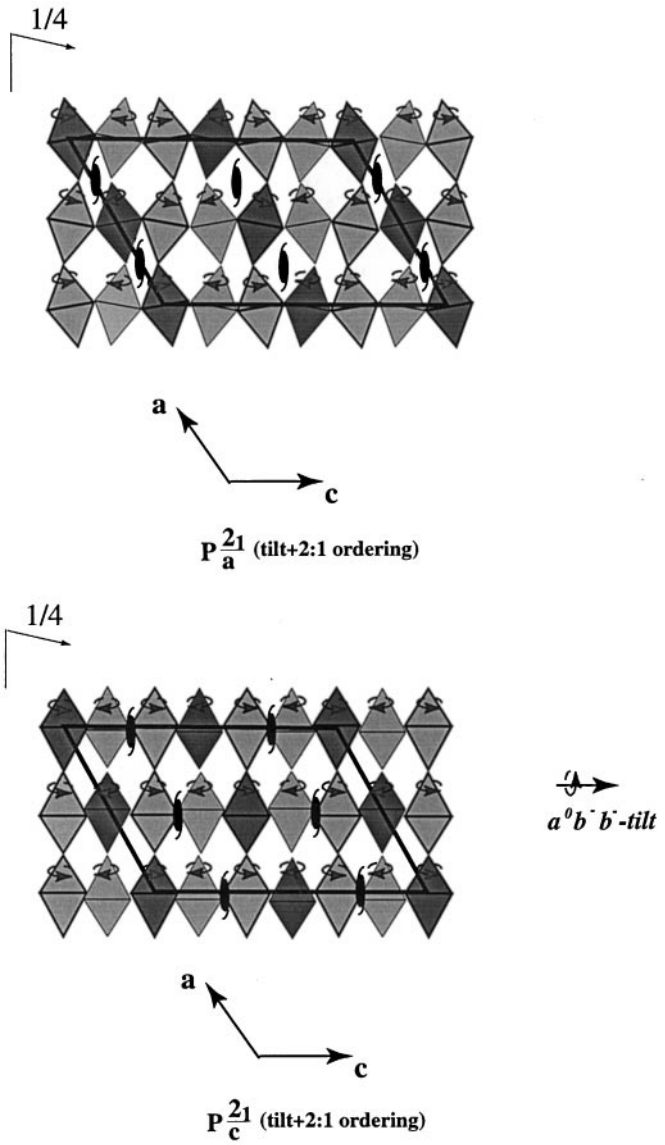

FIG. 20. Schematic $\langle 110\rangle_c$-projections of two possible monoclinic structures resulting from the combination of $a^+b^-b^-$ octahedral tilting and 2:1 cation ordering on *B*-sites. Note the difference in orientation of the ordering vector with respect to the tilting axes.

considerations for the well-separated sequential $\mathbf{C} \rightarrow \mathbf{T}$ and $\mathbf{T} \rightarrow (\mathbf{O}) \rightarrow \mathbf{M}$ transitions. However, for the sequence of continuous symmetry reductions with well-separated $\mathbf{C} \rightarrow \mathbf{T}$ transition, domains **1** and **2** (with orthogonal *c*-axes) are expected to have a strain-free $\{110\}_c$ interface. Formation of zig-zag-like interfaces between domains **1** and **2**, faceted on alternating $(110)_c$ and $(1\bar{1}0)_c$ planes, apparently was effected by the interaction of domains $\mathbf{1}_1$, $\mathbf{1}_2$, $\mathbf{2}_1$ and $\mathbf{2}_2$, and therefore implies the direct $\mathbf{C} \rightarrow \mathbf{M}$ transformation. Alternatively, formation of these zig-zag-like interfaces can be accounted for by the first-order $I4/m$ $(a^0a^0c^-) \rightarrow P2_1/n$ $(b^-b^-c^+)$ or $C2/c$ $(a^0b^-c^+) \rightarrow P2_1/n$ $(b^-b^-c^+)$ transition, accompanied by the change in orientation of the pseudo-tetragonal *c*-axis. Recently, the sequence of $a^0a^0a^0$ $(Pm\bar{3}m) \rightarrow a^0a^0c^-$ $(I4/mcm) \rightarrow a^0b^-c^+$ $(Cmcm) \rightarrow b^-b^-c^+$ $(Pbnm)$ tilting phase transitions has been confirmed for $CaTiO_3$ (4), for which a similar zig-zag-like appearance of $\{110\}$-faceted interdomain boundaries was observed (3). Clearly, high-temperature diffraction data are necessary to determine the exact sequence of tilting phase transitions in $Ca_4Nb_2O_9$.

The space groups of the HTP_2, $LT_{1/4}$, and $LT_{1/6}$ structures are determined by the intersection of *Pbnm* (which describes the symmetry of a $b^-b^-c^+$ tilted octahedral framework) and the translational group imposed by each type of cation ordering. If both a tilting pattern of octahedra and the directions of tilting axes remain unchanged in all three ordered structures, type I and type II domains will be preserved upon the $HTP_2 \rightarrow LT_{1/4}$ and $LT1/4 \rightarrow LT_{1/6}$ transitions. The $HTP_2 \rightarrow LT_{1/4}$ transition formally implies formation of two twin-related monoclinic variants, due to $Pbnm \rightarrow P2_1/c$ symmetry reduction, plus four translational variants, due to a loss of the *c*-glide plane and subsequent doubling of the *c*-lattice parameter. Domains corresponding to these variants were identified in the $LT_{1/4}$ phase (domains III and IV in Fig. 9), and their hierarchy followed that expected from the symmetry analysis. For the $LT1/4 \rightarrow LT_{1/6}$ transition, two twin-related monoclinic domains containing three translational domains were identified within type II domains (Figs. 16 and 17), consistent with the formal transition through the *Pbnm* symmetry state.

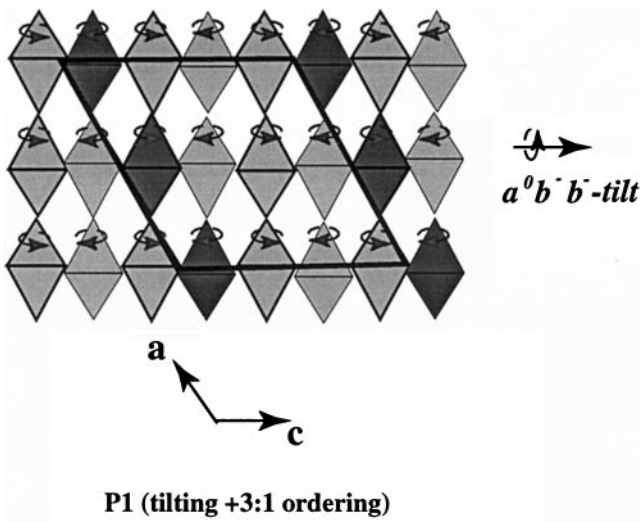

FIG. 21. Schematic $\langle 110\rangle_c$-projection of the triclinic (pseudo-monoclinic) $LT_{1/4}$ structure with a combination of $a^+b^-b^-$ octahedral tilting and 3:1 ordering on *B*-sites. In this model, black and white octahedra refer to the *B*-sites filled exclusively by Ca and by a random mixture of Nb/Ca, respectively. The exact distribution of Ca and Nb cations has yet to be determined by X-ray diffraction Rietveld refinement.

Thus, the microstructural hierarchy suggests that the tilting pattern of octahedra and the directions of tilting axes are preserved in the HTP_2, $LT_{1/4}$, and $LT_{1/6}$ phases. Consequently, the transitions between HTP_2 and the low-temperature structures ($LT_{1/4}$, $LT_{1/6}$), as well as the transition from the metastable, $LT_{1/4}$, to the stable, $LT_{1/6}$, phase are due to reordering of Ca and Nb cations on the *B*-sites. The special orientation relationship between precipitates of the $LT_{1/6}$ ordered phase and the $LT_{1/4}$ matrix is determined by the common orientation of the tilting axes in the octahedral framework.

CONCLUSIONS

Four distinct perovskite-related polymorphs of $Ca_4Nb_2O_9$ were identified with structures that combine octahedral tilting and different ordered arrangements of Ca and Nb cations on *B*-sites. These polymorphs include two high-temperature phases (HTP_1 and HTP_2) existing above $T = 1500$–1600°C and $T = 1400$–1425°C, respectively, and two low-temperature phases that form below $T = 1400$°C. The HTP_1 is either disordered or exhibits 1:1 ordering of Ca and Nb cations on the *B*-sites. In HTP_2, 1:1 ordering is combined with $b^-b^-c^+$ octahedral tilting. Analysis of domain structures and line broadening of X-ray diffraction reflections in quenched specimens suggested that the $HTP_1 \rightarrow HTP_2$ displacive transition occurs between 1500 and 1600°C. The high-temperature form HTP_2 is described by a monoclinic $P2_1/n$ structure with lattice parameters related to that of cubic perovskite according to $\sqrt{2}a_c \times \sqrt{2}a_c \times 2a_c$, with $\beta \approx 90^\circ$. The low-temperature forms of $Ca_4Nb_2O_9$ were described by P1 triclinic and $P2_1/c$ monoclinic structures with lattice parameters $\sqrt{2}a_c \times 2\sqrt{2}a_c \times \sqrt{6}a_c$, $\alpha \approx \gamma \approx 90^\circ$, $\beta \approx 125^\circ$, and $\sqrt{6}a_c \times \sqrt{2}a_c \times 3\sqrt{2}a_c$, $\beta \approx 125^\circ$, respectively. The *P*1 structure exhibited ordering of Ca and Nb cations on *B*-sites with the ordering vector $\mathbf{k} = 1/4[111]^*_c$, but the exact distribution of cations has yet to be determined. This polymorph evolves from the HTP_2 phase on cooling below 1400°C, but is metastable and transforms upon further heating at $T < 1400$°C to the stable $P2_1/c$ phase with 2:1 ordering of Ca and Nb cations. Although the transformation from $P2_1/n$ (1:1 ordered) to the *P*1 structure has some features of a continuous transformation, symmetry analysis indicates that this must be a first-order transition. The transformation from *P*1 to the stable $P2_1/c$ structure is also a first-order transition and occurs by precipitation and growth of the 2:1 ordered phase. Comparison of reciprocal lattices and spatial domain hierarchy indicated that both the tilting pattern of octahedra and the directions of tilting axes are preserved in three of the polymorphs (HTP_2, $LT_{1/4}$, $LT_{1/6}$); that is, all three structures can be described by a combination of the same $b^-b^-c^+$ octahedral tilting with different ordered arrangements of Ca and Nb cations on the *B*-sites. The ordering vectors in the $LT_{1/4}$ and $LT_{1/6}$ structures are preferentially oriented with respect to the tilting axes.

Preliminary evaluation of the dielectric properties of different $Ca_4Nb_2O_9$ polymorphs at frequences above 1 GHz (26) indicated significant variations of the temperature coefficients of the resonant frequencies. Detailed measurements are in progress and will be described elsewhere.

ACKNOWLEDGMENTS

The authors thank D. B. Minor and J. M. Loezos for sample preparation.

REFERENCES

1. H. Kagata and J. Kato, *Jpn. J. Appl. Phys.* **33,** 5463–5465 (1994).
2. H. F. Kay and P. C. Bailey, *Acta Crystallogr.* **10,** 219 (1957).
3. Y. Wang and R. C. Liebermann, *Phys. Chem. Miner.* **20,** 147–158 (1993).
4. B. J. Kennedy, C. J. Howard, and B. C. Chakoumakos, *J. Phys. Condensed Matter* **11**(6), 1479–1488 (1999).
5. M. Hervieu, F. Studer, and B. Raveu, *J. Solid State Chem.* **22,** 273–289 (1977).
6. A. C. Larson and R. B. Von Dreele, "General Structure Analysis System," Los Alamos National Laboratory Report LAUR 86-748, 1994.
7. J. P. Cline, *in* "Industrial Applications of X-Ray Diffraction" (F. H. Chung and D. K. Smith, Ed.), pp. 903–917. Dekker, New York, 1994.
8. T. Hahn, Ed., "International Tables of Crystallography." Kluwer Academic, Dordrecht/Norwell, MA, 1995.
9. H. D. Megaw, "Crystal Structures: A Working Appoach." Saunders, Philadelphia, 1973.
10. A. M. Glaezer, *Acta Crystallogr.* **B31,** 2129–2130 (1975).
11. K. S. Alexandrov, *Ferrolectrics* **14,** 801–805 (1976).
12. P. M. Woodward, *Acta Crystallogr.* **B53,** 32–43 (1997).
13. P. M. Woodward, *Acta Crystallogr.* **B53,** 44–66 (1997).
14. L. Chai and P. Davies, *J. Am. Ceram. Soc.* **80**(12), 3193–3198 (1997).
15. M. Hervieu, B. Raveau, J. Lecompte, and J. P. Loup, *Rev. Chim. Miner.* **22**(1) 44–57, (1985).
16. M. Couzi, S. Khairoun, and A. Tressaud, *Phys. Status Solidi A* **98,** 423–434 (1986).
17. K. S. Alexandrov, S. V. Melnikova, and S. V. Misyul, *Phys. Status Solidi A* **104,** 545–548 (1987).
18. A. R. Chakhmouradian and R. H. Mitchell, *J. Solid State Chem.* **138,** 272–277 (1998).
19. I. D. Brown and D. Altermatt, *Acta Crystallogr.* **B41,** 244–247 (1985).
20. K. S. Alexandrov, *Ferroelectrics* **14,** 801–805 (1976).
21. C. J. Howard and H. T. Stokes, *Acta Crystallogr.* **B54,** 782–789 (1998).
22. M. T. Anderson, K. B. Greenwood, G. A. Taylor, and K. R. Poeppelmeier, *Prog. Solid State Chem.* **22**(3), 197–233 (1993).
23. F. Galasso and J. Pyle, *Inorg. Chem.* **2,** 483 (1963).
24. R. S. Roth, to be published, 1999.
25. J. Sapriel, *Phys. Rev. B* **12**(11), 5128–5140 (1975).
26. R. Geyer, private communication.